Chlorin e6-Loaded Nanostructured Lipid Carriers Targeted by Angiopep-2: Advancing Photodynamic Therapy in Glioblastoma

Carlotta Pucci,* Daniele De Pasquale,* Andrea Degl'Innocenti,* Margherita Montorsi, Andrea Desii, Marta Pero, Chiara Martinelli, Martina Bartolucci, Andrea Petretto, and Gianni Ciofani*

Glioblastoma (GBM) is a highly aggressive brain tumor known for its resistance to standard treatments. Despite surgery being a primary option, it often leads to incomplete removal and high recurrence rates. Photodynamic therapy (PDT) holds promise as an adjunctive treatment, but safety concerns and the need for high-power lasers have limited its widespread use. This research addresses these challenges by introducing a novel PDT approach, using chlorin e6 (Ce6) enclosed in nanostructured lipid carriers (Ang-Ce6-NLCs) and targeted to GBM with the angiopep-2 peptide. Remarkably, a single 5-min irradiation session with LEDs at 660 nm and low power density (10 mW cm^{-2}) proves effective against GBM, while reducing safety risks associated with high-power lasers. Encapsulation improves Ce6 stability and performance in physiological environments, while angiopep-2 targeting enhances delivery to GBM cells, maximizing treatment efficacy and minimizing off-target effects. The findings demonstrate that Ang-Ce6-NLCs-mediated PDT brings about a significant reduction in GBM cell viability, increases oxidative stress, reduces tumor migration, and enhances apoptosis. Overall, such treatment holds potential as a safe and efficient intraoperative removal of GBM infiltrating cells that cannot be reached by surgery, using low-power LED light to minimize harm to surrounding healthy tissue while maximizing tumor treatment.

1. Introduction

Glioblastoma (GBM) is the deadliest form of brain cancer, with a low survival rate and limited treatment options.[1] Standard treatments like surgery, chemotherapy, and radiotherapy have limited efficacy and severe side effects. GBM has a highly invasive nature, making complete surgical removal difficult and leading to high recurrence rates (≈90%) and short life expectancy (with a median survival of 12–15 months, and a 5-year survival of ≈5%).[2] GBM genetic variability poses challenges in the selection of the correct therapeutic regimen for each patient.[2] Furthermore, GBM exhibits a high capacity to infiltrate healthy brain tissues, making the precise identification and removal of tumor cells challenging.[3] Finally, the blood–brain barrier (BBB) hinders the delivery of anticancer drugs to the tumor.[4] It appears clear that new therapeutic approaches are urgently needed to fight this incurable tumor.

C. Pucci[+], D. De Pasquale, A. Degl'Innocenti[++], M. Montorsi[+++],
A. Desii, C. Martinelli[++++], G. Ciofani
Istituto Italiano di Tecnologia
Smart Bio-Interfaces
Viale Rinaldo Piaggio 34, Pontedera 56025, Italy
E-mail: carlotta.pucci@santannapisa.it; daniele.depasquale@iit.it; andrea.deglinnocenti@unisi.it; gianni.ciofani@iit.it

The ORCID identification number(s) for the author(s) of this article can be found under https://doi.org/10.1002/adhm.202402823

[+]Present address: Scuola Superiore Sant'Anna, The BioRobotics Institute, Viale Rinaldo Piaggio 34, Pontedera 56025, Italy

[++]Present address: Università degli Studi di Siena, Department of Medical Biotechnologies, Via Aldo Moro 2, Siena 53100, Italy

[+++]Present address: IPCF-CNR, Sede secondaria di Pisa, Largo Bruno Pontecorvo 3, Pisa 56127, Italy

[++++]Present address: Politecnico di Milano, Department of Chemistry, Materials Chemical Engineering "Giulio Natta", Piazza Leonardo da Vinci, 32, Milano 20133, Italy

M. Montorsi[+++]
Scuola Superiore Sant'Anna
The BioRobotics Institute
Viale Rinaldo Piaggio 34, Pontedera 56025, Italy

M. Pero
Politecnico di Torino
DIMEAS
Corso Duca degli Abruzzi 24, Torino 10129, Italy

M. Bartolucci, A. Petretto
IRCCS Istituto Giannina Gaslini
Core Facilities-Clinical Proteomics and Metabolomics
Via Gerolamo Gaslini 5, Genova 16147, Italy

Photodynamic therapy (PDT) has emerged as a valuable modality for tumor treatment, particularly useful for genetically diverse tumors, like GBM. PDT activates a photosensitizer with light at a specific wavelength to generate reactive oxygen species (ROS) that induce tumor cell death.[5] Photosensitizers are generally nontoxic in the absence of light, facilitating precise localization of the treatment to the stimulated area. The broad-spectrum cytotoxicity of ROS renders them effective across various tumor characteristics and genetic profiles. The activation of the photosensitizer needs an optimal energy input, typically achieved by high-power laser light sources; however, high-power lasers raise concerns about potential damage to healthy tissues. Moreover, due to laser small irradiance area, the complete ablation of all tumor cells usually requires long treatment sessions. Thus, there is a demand for novel photosensitizers, capable of efficiently generating ROS with low-energy stimulations and offering a potential solution to enhance the efficacy and safety of PDT applications.

Chlorophyll derivates show promise for PDT due to their unique characteristics: they have low dark toxicity, they are easily eliminated from the body, and they absorb light in a range where interference from hemoglobin and melanin absorption has lower impact (650–800 nm), enabling the stimulation of regions located deeper than a few millimeters, and they produce ROS with a high yield, suggesting the potential to reduce the power required for their stimulation.[6] Chlorin e6 (Ce6), a chlorophyll derivative belonging to the chlorins family (i.e., 18π-electron aromatic compounds with a tetrapyrrole backbone possessing two extra hydrogens compared to porphyrins[7]), stands out for its advancement in clinical studies thanks to its low dark toxicity, fast clearance,[8] light absorption between 650 and 670 nm, a singlet oxygen quantum yield of 0.7 (in phosphate buffer),[9] and a triplet lifetime of 760 μs.[7] Nevertheless, Ce6, like many chlorophyll derivatives, exhibits low solubility in biological fluids, forming aggregates that have a negative impact on their optical and photodynamic properties.[6] In this context, nanomedicine has fostered the development of nanoparticles as carriers for chlorophyll derivatives, enabling their targeted delivery, improving their bioavailability, and favoring the stability of their optical properties in biological environments.

Our study introduces a nanotechnological approach for delivering Ce6 to GBM using angiopep-2 (Ang)-functionalized nanostructured lipid carriers (NLCs, Ang-bearing, and Ce6-loaded NLCs being referred to as Ang-Ce6-NLCs). These nanoparticles serve as a biocompatible and biodegradable delivery system, preventing Ce6 aggregation in biological media and preserving its optical properties, ensuring optimal ROS production upon light exposure. Surface modification with Ang enhances targeting to GBM cells, leveraging its interaction with the low-density lipoprotein receptor-related protein 1 (LRP1) overexpressed on GBM cell membranes.[10]

To investigate ROS production and PDT from Ang-Ce6-NLCs interaction with light, we designed a specific LED stimulator (660 nm) with precise geometry for uniform irradiation over a large area. This novel set-up allows simultaneous irradiation of multiple samples on conventional multi-well plates, advancing high-throughput screening in PDT research. Additionally, it also accommodates a custom fluidic bioreactor mimicking an in vitro neurovascular unit (NVU) affected by GBM, comprising a BBB model (brain endothelial cells, human astrocytes, and pericytes)

and healthy brain cells (neurons, microglia, and astrocytes) in co-culture with GBM cells. Thanks to these tools, we showed that Ang-Ce6-NLCs effectively generate ROS and induce GBM cell death with just 5 min of light exposure at low power density (10 mW cm^{-2}). Importantly, Ang-Ce6-NLCs-mediated PDT exhibited selective action on GBM cells, even when the entire NVU model was under light exposure. A schematic representation of the experimental design proposed in our work is presented in Figure S1 (Supporting Information).

Our Ang-Ce6-NLCs obviate the need for costly laser stimulations, utilizing a more accessible LED set-up for PDT and GBM ablation. Moreover, LEDs offer the advantage of irradiating a larger area, allowing in situ tumor cavity stimulation during surgical resection. At the same time, the selective action of Ang-Ce6-NLCs ensures specific removal of invaded GBM cells that cannot be easily reached by surgery,[11] while ensuring minimal impact on healthy cells.

2. Results and Discussion

2.1. Nanoparticles Characterization

The morphology and size of the nanoparticles were assessed by transmission electron microscopy (TEM) (**Figure** 1A,B; Figure S2A,B, Supporting Information). Both Ce6-NLCs and Ang-Ce6-NLCs display a spherical morphology; the functionalization with Ang has no impact on the overall morphology, in agreement with previous works.[12] The mean diameters of the nanoparticles were determined to be 96 ± 2 nm for Ce6-NLCs and 97 ± 4 nm for Ang-Ce6-NLCs. The hydrodynamic diameters were also measured by dynamic light scattering (DLS) to be 224 ± 11 nm for Ce6-NLCs and 194 ± 4 nm for Ang-Ce6-NLCs, confirming the little impact of the functionalization on the nanoparticle size. Moreover, the low polydispersity index (0.212 ± 0.005 for Ce6-NLCs and 0.184 ± 0.012 for Ang-Ce6-NLCs) and the presence of a single population in the intensity distribution in Figure S2C (Supporting Information) suggest a fairly monodisperse sample. The ζ-potential of Ang-Ce6-NLCs is slightly higher (−23.8 ± 0.5 mV) than that of Ce6-NLCs (−28.3 ± 0.7 mV), suggesting a partial screening of the surface charges due to the Ang functionalization. This result agrees with previous studies on PEGylated lipid nanoparticles functionalized with the same peptide.[12]

To confirm the successful functionalization of the nanoparticles with Ang, Sodium dodecyl sulfate-poly(acrylamide) gel electrophoresis (SDS-PAGE) followed by Coomassie staining was performed (Figure S2D, Supporting Information). Ang-Ce6-NLCs display a band, similar to that found running Ang alone, confirming the presence of the peptide on the nanoparticles; on the other hand, bare Ce6-NLCs do not give rise to any band after the staining, validating the specificity of the test for the peptide, with no interference from other components of the nanoparticles. After comparing the intensity of the band of Ang-Ce6-NLCs with that of a known amount of peptide alone, the percentage of Ang attached to the surface of the nanoparticles was found to be 2.6 ± 0.6 wt%.

The stability of Ang-Ce6-NLCs in terms of their hydrodynamic diameter was assessed in different buffers, particularly in water (storage conditions), at pH 7.4 (phosphate buffer saline, PBS) to replicate physiological conditions, at pH 4.5 (phosphate
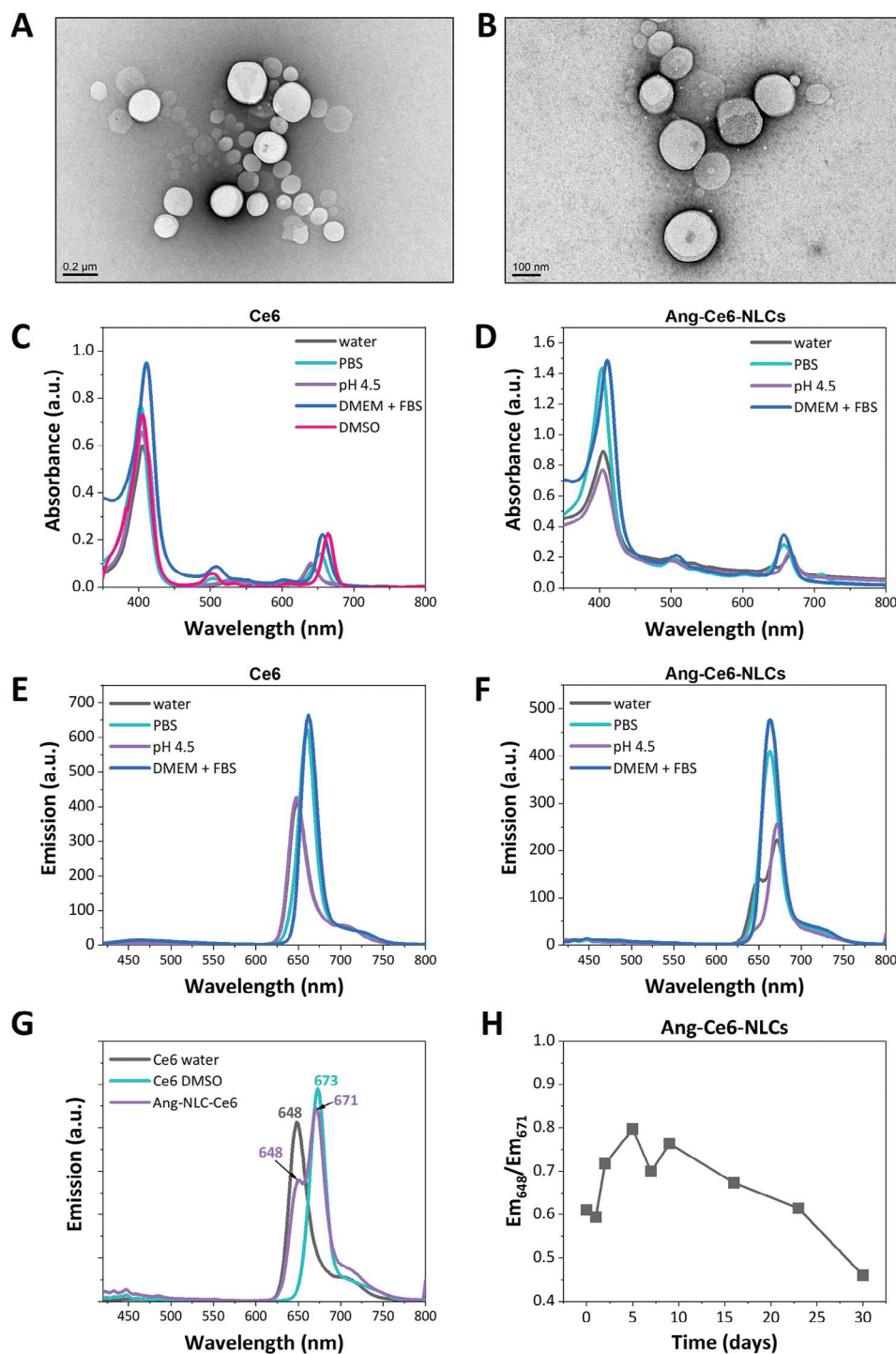
**ADVANCED
SCIENCE NEWS**

www.advancedsciencenews.com

**ADVANCED
HEALTHCARE
MATERIALS**

www.advhealthmat.de

Figure 1. TEM images of A) Ce6-NLCs and B) Ang-Ce6-NLCs. C) UV/visible spectra of Ce6 in water (gray), PBS (cyan), at pH 4.5 (violet), DMEM + FBS (blue). D) UV/visible spectra of Ang-Ce6-NLCs in water (gray), PBS (cyan), at pH 4.5 (violet), DMEM + FBS (blue). E) Fluorescence emission spectra (λex 405 nm) of Ce6 in water (gray), PBS (cyan), at pH 4.5 (violet), DMEM + FBS (blue). F) Fluorescence emission spectra (λex 405 nm) of Ang-Ce6-NLCs in water (gray), PBS (cyan), at pH 4.5 (violet), DMEM + FBS (blue). G) Fluorescence emission spectra (λex 405 nm) of Ce6 in water (gray), Ce6 in DMSO (cyan), and Ang-Ce6-NLCs in water. H) Emission at 648 nm over the emission at 671 nm of Ang-Ce6-NLCs in water over time (λex 405 nm).

Table 1. Absorption maxima of Ce6 and Ang-Ce6-NLCs in different buffers.

Buffer	Ce6		Ang-Ce6-NLCs	
	Soret Band [nm]	Q_y Band [nm]	Soret Band [nm]	Q_y Band [nm]
DMSO	406	664		
Water	405	640	405	666
PBS	403	653	404	657
pH 4.5	403	640	405	666
DMEM + FBS	410	656	410	657

Table 2. Emission maxima of Ce6 and Ang-Ce6-NLCs in different buffers (λex 405 nm).

Buffer	Ce6	Ang-Ce6-NLCs
	Emission [nm]	Emission [nm]
Water	648	648, 671
PBS	661	663
pH 4.5	648	672
DMEM + FBS	661	663

buffer) to mimic the conditions within tumor microenvironment or acidic organelles, and in high-glucose Dulbecco's Modified Eagle Medium (DMEM) supplemented with 10% fetal bovine serum (FBS) (here called, DMEM + FBS), representing the final dispersing medium of the nanoparticles when administered to cells.[13,14] All these conditions, except for water, were also replicated in the presence of 100 µM hydrogen peroxide (H_2O_2), to mimic the higher oxidative stress conditions within cancer cells.[15] As shown in Figure S2E (Supporting Information), the hydrodynamic diameter of Ang-Ce6-NLCs remains fairly stable in all the conditions studied, throughout the whole considered timeframe (30 days).

The loading of Ce6 within Ang-Ce6-NLCs was measured by high-performance liquid chromatography (HPLC) to be 0.7 ± 0.1 wt% and confirmed by fluorescence spectroscopy, which suggested a Ce6 loading equal to 1.1 ± 0.4 wt%. From these two measurements, we could also determine that the encapsulation efficiency of Ce6 in the nanoparticles is around 25–39%.

The optical properties of free Ce6 and Ang-Ce6-NLCs were measured by UV/visible and fluorescence spectroscopy to elucidate the impact of Ce6 encapsulation within the lipidic core. Absorption spectra of free Ce6 were collected in different media and compared to those of Ang-Ce6-NLCs (Figure 1C,D). Similarly to other chlorophyll derivatives, Ce6 spectrum is characterized by three main bands (Figure 1C): the Soret bands at lower wavelengths (≈ 400–410 nm), and the Q_x and Q_y bands at longer wavelengths (≈ 450–550 and 640–660 nm, respectively). According to Gouterman's four-orbital model, the emergence of the Soret band stems from electronic transitions from the ground state (S_0) to higher excited singlet states (S_n), while the Q bands originate from the excitation of lower excited singlet states (S_1).[16–18] The position of these bands, particularly the Q_y band, strongly depends on the environment and the aggregation state of Ce6.[16] In aqueous solutions, the limited solubility of chlorophyll derivatives, owing to their inherent hydrophobic nature due to the heterocyclic ring structure, fosters their aggregation into supramolecular complexes. Two types of aggregates can form: J-aggregates, characterized by a dimer alignment angle smaller than 54.7°, and H-aggregates, featuring an angle larger than 54.7°. These aggregations significantly influence the optical properties of Ce6; J-aggregates induce a red-shift in the Q bands, while H-aggregates result in their blue shift relative to the monomeric form of Ce6.[16] As evidenced in Figure 1C and **Table 1**, the absorption spectrum of Ce6 in dimethyl sulfoxide (DSMO) shows a Soret band at 406 nm and a Q_y band at 664 nm. Since Ce6 is soluble in DMSO, under such conditions, Ce6 predominantly exists in its

monomeric form. However, when dissolved in aqueous solvents, a blue-shift of the Q_y band is observed, indicating partial aggregation into H-aggregates. Both in water and in buffer at pH 4.5, the Qy band experiences a blue-shift at 640 nm ($\Delta\lambda = 24$ nm), while in PBS and DMEM + FBS, the band shifts to 653 ($\Delta\lambda = 11$ nm) and 657 nm ($\Delta\lambda = 7$ nm), respectively. Although the observed $\Delta\lambda$ suggest slightly better compatibility of Ce6 with basic environments, all conditions demonstrate a shift relative to Ce6 in DMSO, denoting poor solubility in all buffers. Upon encapsulation in Ang-Ce6-NLCs, Ce6 optical properties deviate from those of the free molecule in the same solvents (Figure 1D and Table 1). Although the Soret band appears unaffected by encapsulation, the Q_y band of Ce6 in Ang-Ce6-NLCs dispersed in water and at pH 4.5 (≈666 nm) closely resembles that observed in DMSO. Conversely, when dispersed in PBS or DMEM + FBS, the Q_y band position aligns with that of free Ce6 in the same solvents. As reported in the literature, the solubility of Ce6 in aqueous environments is pH-dependent, with higher pH values enhancing its solubility through deprotonation of the carboxyl groups.[19] Thus, when Ang-Ce6-NLCs are dispersed under slightly acidic conditions (water and pH 4.5), Ce6 predominantly remains well-encapsulated within the nanoparticle in a monomeric form. In contrast, a more basic pH (PBS and DMEM + FBS) renders the environment less harsh for Ce6, likely leading to some degree of Ce6 exposure to the solvent and consequent aggregation.

To further substantiate this observation, the fluorescence emission of Ce6 and Ang-Ce6-NLCs in different conditions was measured (Figure 1E–G and **Table 2**). When Ce6 is dissolved in DMSO, its peak emission occurs at 673 nm (λex 405 nm). However, in water and at pH 4.5, the peak shifts to lower wavelengths (648 nm, $\Delta\lambda = 25$ nm), while in PBS or DMEM + FBS it shifts less prominently to 661 nm ($\Delta\lambda = 12$ nm), consistently with the trends of the UV/visible spectra. In Ang-Ce6-NLCs, the maximum emission aligns with that of free Ce6 in PBS or DMEM + FBS, while at pH 4.5, the peak precisely reflects that of free Ce6 in DMSO, corroborating UV/visible findings. Interestingly, in water the emission peak comprised two main contributions at 648 nm (like free Ce6 in DMSO) and 671 nm (like free Ce6 in water), suggesting a dual distribution of Ce6 within the nanoparticles (Figure 1G). One Ce6 fraction might reside in a monomeric state within the lipid core, akin to the organic solvent environment, while another might be predominantly at the periphery of the lipid core, influenced by the aqueous solvent near the poly(ethylene glycol) (PEG) hydrophilic chain. This observation underscores the complex dynamics of Ce6 encapsulation within Ang-Ce6-NLCs and its response to different environmental cues. A similar Ce6 partitioning in small unilamellar vesicles was

2402823 (4 of 25)

**ADVANCED
SCIENCE NEWS**

www.advancedsciencenews.com

**ADVANCED
HEALTHCARE
MATERIALS**

www.advhealthmat.de

observed by Frolov et al. studying the optical properties of Ce6.[20] The authors reported a red-shift of approximately 6 nm in absorption and fluorescence spectra for Ce6 in a lipid environment compared to weak alkaline solutions (pH 7.4), consistent with our findings. They also found a similarity in Ce6 fluorescence decay time between liposomes and organic solvents with dielectric constants ranging from 12 to 20. This led them to suggest Ce6 localization at the lipid/water interface of the lipid membrane, interacting with phospholipid glycerine residues and assuming a fixed position at the membrane boundary, between the polar and non-polar region.[20] Ce6 partitioning between aqueous and lipid phases is influenced by the properties of the polar phase;[21] higher acidity corresponds to a greater Ce6 fraction in the non-polar phase., i.e., the lipid phase. Accordingly, in our results, at pH 4.5, UV/visible and fluorescence spectra of Ang-Ce6-NLCs resemble those of free Ce6 in DMSO, as Ce6 partition in the lipid phase increases. While our nanoparticles structurally differ from liposomes, the presence of 1,2-distearoyl-*sn*-glycero-3-phosphoethanolamine (DSPE) phospholipid covalently linked to PEG may create an environment akin to the lipid/solvent interface seen in liposomes. This suggests a potential similarity in Ce6 behavior within Ang-Ce6-NLCs and liposomes.

To determine whether Ce6 partitioning within the nanoparticle evolves over time, we observed the fluorescence emission of Ang-Ce6-NLCs in water and performed peak deconvolution to distinguish contributions from polar and non-polar fractions (Figure S3, Supporting Information). As depicted in Figure 1G, within the initial 5 days post-dispersion in water at 37 °C, there was a discernible increase in Ce6 partitioning into the aqueous phase, indicating progressive redistribution.

The optical properties of Ang-Ce6-NLCs were also investigated in the presence of an oxidizing agent (hydrogen peroxide 100 μM) to simulate the more oxidative microenvironment of cancer cells; nevertheless, no difference was found with respect to the same buffers without hydrogen peroxide (Figure S4 and Table S1, Supporting Information).

Another crucial aspect of chlorophyll derivatives used in PDT is the potential degradation of their optical properties over time. Previous studies have shown that the formation of aggregates and increased $\pi-\pi$ stacking can result in fluorescence quenching and reduced photodynamic activity.[16] To address this concern, we monitored the absorption and fluorescence spectra of both free Ce6 and Ang-Ce6-NLCs in various buffers over a 30-day period. As illustrated in Figures S5–S7 (Supporting Information), aside from the already discussed redistribution of the emission peaks observed in Ang-Ce6-NLCs in water, there were no significant changes in the spectral shape over time in all conditions. However, a notable decrease in intensity was observed. To elucidate this phenomenon further, we calculated the ratio of emission intensity at each time point (I) to the intensity at the beginning of the study (time zero, I_0; Figure S8, Supporting Information). In all conditions, a reduction in emission intensity was observed for both Ce6 and Ang-Ce6-NLCs. Notably, the fluorescence quenching was consistently less pronounced when Ce6 was encapsulated in the nanoparticles, suggesting a protective role of the nanoparticles in mitigating the formation of detrimental aggregates. This effect was particularly pronounced in water and acidic conditions, where Ce6 insolubility led to a complete loss of function of the free molecule.

2.2. LED-Stimulation Set-Up

For consistent stimulation during LED irradiation, we developed a dedicated LED stimulator set-up accommodating 24-well plates for in vitro experiments and fluidic bioreactors for advanced multi-culture studies (**Figure 2**A). The chamber comprises a box housing a row of seven 660 nm-LEDs positioned at the bottom, on a metallic bar to prevent LED overheating. A power controller regulates the voltage supply to the LEDs, ensuring precise control over power density at the multi-well bottom (Figure S9A, Supporting Information). The chamber temperature during 5-min irradiation at 10 mW cm^{-2} showed no significant variations from room temperature (Figure S9B, Supporting Information).

Mathematical simulations were conducted to better characterize the light distribution within the LED stimulator set-up, aiming to optimize the radiant intensity across the 24-well plate and from the LEDs to the multi-well bottom. Under stationary conditions, light fluence distribution was simulated and visualized using 3D or 2D color maps alongside 1D line plots. The geometrical model used in the simulation (Figure 2B) reproduced the real illumination set-up employed for cell experiments, with seven hemispheres ($R = 1.53$ mm) representing the LED heads positioned on the bottom chamber surface, while the polystyrene (PS) 24-well plate is placed 2.7 cm above the LEDs. Figure 2C represents the 2D color map of light fluence on the 24-well plate bottom surface for a radiant flux of 682.5 mW from LED sources. In the central wells directly above LEDs, light fluence reaches 3.8 mW cm^{-2}. The difference in light fluences among the wells and the PS surrounding walls is attributed to the second reflection phenomena due to refractive index mismatch between PS and the cell medium. In Figure 2D, line plots of the light fluence across adjacent wells for different LED radiant flux clearly demonstrate higher intensities in the central wells with respect to the lateral ones. According to these results, in this work all stimulations were conducted by positioning the samples only in the central wells, to guarantee homogenous irradiation to all the experimental classes. At simulated LED radiant flux (1312 mW), light fluence at the central wells reaches 6.7 mW cm^{-2}, adjustable by increasing LED current supply. Figure 2E shows the light fluence 3D color map related to the entire geometric model. In the bottom chamber, light fluence is homogenous, as the air medium does not affect light propagation at this wavelength.[22,23] Conversely, light intensity exponentially decreases at the PS multi-well boundary, adhering to the Robin boundary condition. Line plots in Figure 2F show an exponential decay of the light fluence across the PS layer, for different LED radiant flux related to the segment connecting the central LED with the middle well, resulting in light transmission of 35%.

Accounting for these phenomena is crucial in PDT to adjust LED voltage input based on the desired power density required for effective sample irradiation. This numerical finite element method (FEM) model confirms the suitability of our LED-based cell stimulation set-up at 660 nm. Moreover, it paves the way for carrying out simulation studies on soft biological tissue, helping further investigations into the potential application of PDT in vivo. By adjusting the optical properties of the involved light diffusion media, such as those of the dermis or other tissues, one can optimize light source flux parameters to achieve the desired light excitation intensity, enhancing the therapy's effectiveness.[24,25]
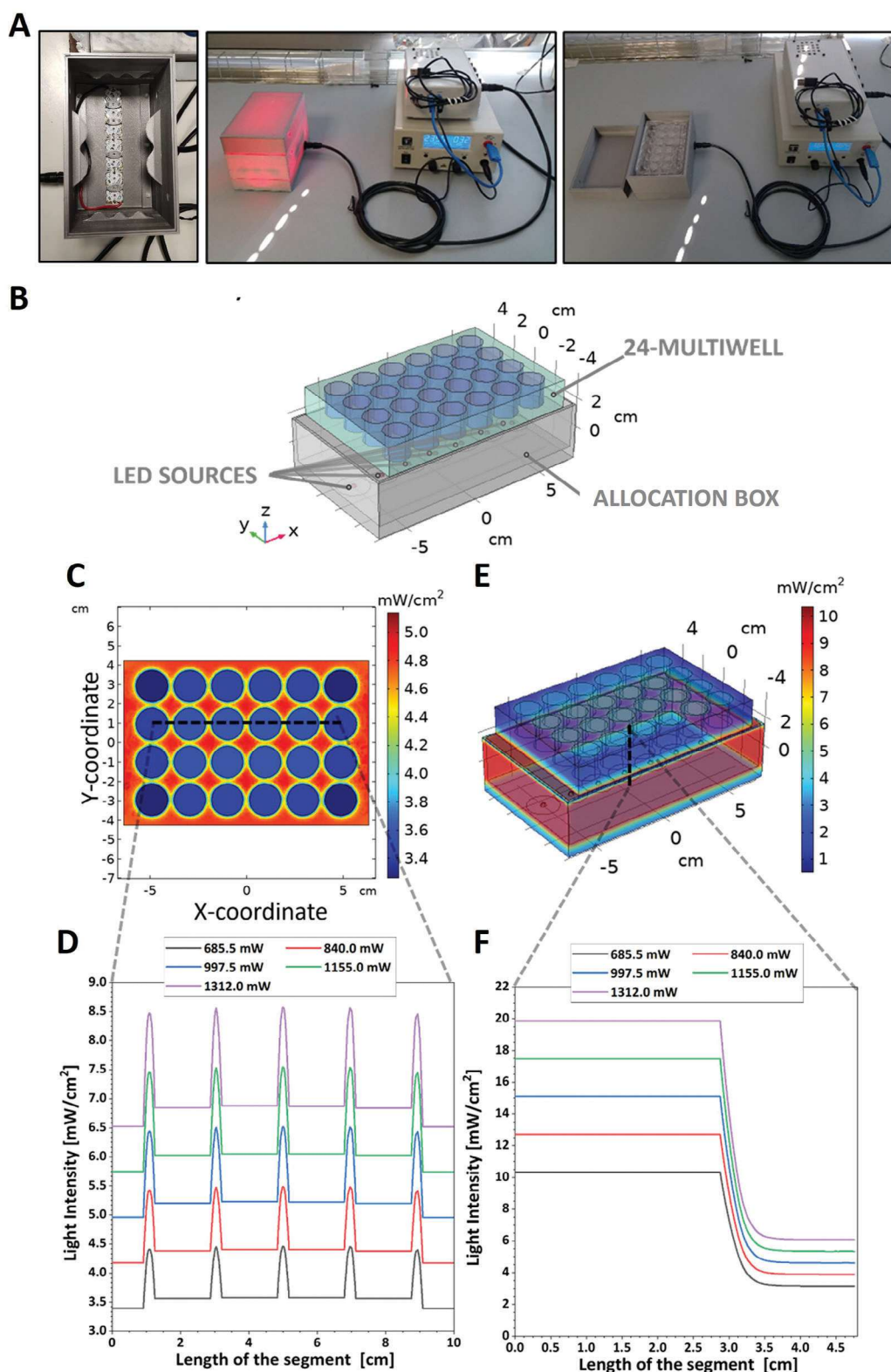
**ADVANCED
SCIENCE NEWS**

www.advancedsciencenews.com

**ADVANCED
HEALTHCARE
MATERIALS**

www.advhealthmat.de

Figure 2. A) Images of the LED irradiation set-up. B) Schematic representation of the set-up. C) 2D color map of light fluence on the 24-well plate bottom surface for a radiant flux of 682.5 mW. D) Light fluence (mW cm^{-2}) across adjacent wells for different LED radiant flux. E) Light fluence 3D color map in the entire model. F) Light fluence (mW cm^{-2}) for different radiant fluxes from the central LED to the middle well.

**ADVANCED
SCIENCE NEWS**
www.advancedsciencenews.com

**ADVANCED
HEALTHCARE
MATERIALS**
www.advhealthmat.de

2.3. ROS Production Upon Ang-Ce6-NLCs Light Stimulation and Release of Ce6 from Ang-Ce6-NLCs

For effective PDT, the photosensitizer must generate singlet oxygen and reactive oxygen species upon exposure to suitable radiation, preferably in the far-red visible spectrum for enhanced tissue penetration and therapeutic efficacy.[6] According to Ce6 absorption spectrum, it can be stimulated both at 405 nm (Soret band) and at 660 nm (Q_y band) to trigger PDT.[26]

To assess Ang-Ce6-NLCs singlet oxygen production upon light stimulation, we evaluated the effect on the absorption of 1,3-diphenylisobenzofuran (DPBF) during Ang-Ce6-NLCs irradiation (Figure S10A, Supporting Information). DPBF absorbs light at 415 nm but reacts with singlet oxygen to form o-dibenzoylbenzene, which does not absorb light.[27] Thus, the reduction in DPBF absorption intensity at 415 nm directly reflects singlet oxygen production in the presence of a photosensitizer. Despite partial overlap with Ce6 Soret band, a distinct shoulder at 415 nm attributed solely to DPBF allows its use for assessing Ce6 photodynamic activity (Figure S10B, Supporting Information). In Figure S10A (Supporting Information), stimulation of DPBF without a photosensitizer or with empty lipid nanoparticles (Ang-NLCs) showed no notable difference in intensity. However, when either free Ce6 or Ang-Ce6-NLCs were combined with DPBF, a reduction in intensity occurred upon stimulation at 660 nm, indicating singlet oxygen production. Specifically, a reduction of $34 \pm 7\%$ for Ce6 and $31 \pm 2\%$ for Ang-Ce6-NLCs with respect to DPBF absorption before light stimulation was measured ($p < 0.01$). Additionally, the absence of interference from individual components (DMSO, Ang-NLCs, Ce6, and Ang-Ce6-NLCs) without DPBF was verified, ruling out the influence of Ce6 Soret band on DPBF absorption measurement (Figure S10C, Supporting Information). Samples with DPBF were also stimulated with LED at 405 nm (Figure S10D, Supporting Information), showing a decrease in DPBF absorption intensity only in the presence of Ce6 or Ang-Ce6-NLCs. Notably, regardless of the excitation wavelength, both Ce6 and Ang-Ce6-NLCs exhibited similar effects on DPBF quenching. The experiment conducted in DMSO due to DPBF insolubility in aqueous environments suggests the dissolution of the Ang-Ce6-NLCs nanoparticle core, dispersing previously encapsulated Ce6 in the solvent at the same concentration as free Ce6. Thus, the similarity in photodynamic activity between Ce6 and Ang-Ce6-NLCs for this test is not surprising.

To probe the efficacy of Ang-Ce6-NLCs in aqueous environments, resembling real application scenarios, the evaluation of singlet oxygen generation under light stimulation was also investigated with the Singlet Oxygen Sensor Green (SOSG) probe. SOSG displays a weak blue fluorescence, with excitation peaks observed at 372 and 393 nm, and emission peaks at 395 and 416 nm. Upon interaction with singlet oxygen, strong green fluorescence ($\lambda_{ex}/\lambda_{em}$ 504/525 nm) is produced. Monitoring the fluorescence increase of SOSG post-light exposure allows an estimation of the photosensitizer photodynamic activity. ROS are highly reactive chemicals that quickly react with their environment. Encapsulation of Ce6 within a nanocarrier may influence ROS concentration available for cellular damage, as they can be readily consumed through interactions with lipids within the nanoparticles. In aqueous and physiological environments,

where the nanoparticles remain intact, the observed effects on singlet oxygen production stem from Ce6 encapsulation within the nanoparticles and can give more information about the potentiality of Ang-Ce6-NLCs for PDT. **Figure 3A** illustrates that, despite being encapsulated within Ang-Ce6-NLCs, Ce6 retained its capability to generate singlet oxygen upon stimulation at 660 nm, inducing an increase of $\approx192 \pm 80\%$ in SOSG emission compared to the probe alone ($p < 0.05$). Notably, its activity appears slightly enhanced compared to free Ce6 ($64 \pm 6\%$, $p < 0.05$). This enhancement could be attributed to the aggregation state of free Ce6 in aqueous environments, influencing its fluorescence and photodynamic activity, as discussed earlier. Thus, encapsulation within lipid nanoparticles effectively preserves Ce6 optical properties and photodynamic activity in physiological environments. Similarly to the DPBF quenching test, the SOSG assay was also conducted by stimulating the samples at 405 nm for comparison (Figure S10E, Supporting Information). However, no statistically significant difference between free Ce6 and Ang-Ce6-NLCs was observed at this wavelength. This may be due to the higher energy associated with the 405 nm wavelength, potentially compensating for any efficiency loss due to Ce6 aggregation in aqueous environments. Nonetheless, due to its reduced tissue penetration and potential toxicity, the 405 nm wavelength is unsuitable for clinical applications, leading us to focus solely on the 660 nm wavelength for further experiments.

The photodynamic properties of photosensitizers involve transitions from the ground state (S_0) to short-lived excited states (S_n) upon light excitation. Subsequent non-radiative decay leads to the first excited state (S_1) via internal conversion, potentially transitioning to the triplet state (T_1) via an intersystem crossing.[6] Among the various pathways available for returning to the ground state, photosensitizers can transfer energy to their surrounding environment. Type I reactions involve energy transfer to molecular substrates, producing radical species that react with oxygen to form ROS, notably hydroxyl radicals and hydrogen peroxide. Type II reactions directly transfer energy to ground triplet state oxygen, forming singlet oxygen. In PDT, it is assumed that Type II reactions are the predominant mechanism.[16] However, the generation of other species through Type I reactions is always possible. To discern the involved mechanisms and understand ROS generation upon Ce6 or Ang-Ce6-NLCs stimulation, we conducted SOSG experiments with the ROS scavengers histidine and mannitol. Histidine is known to scavenge both hydroxyl radicals and singlet oxygen;[28] thus, regardless of the energy transfer mechanism, the gain of fluorescence emission at 525 nm of SOSG should be prevented in the presence of histidine. In our experiments, the presence of histidine effectively prevented the increase of SOSG fluorescence in both Ang-Ce6-NLCs and Ce6 alone upon light stimulation (Figure 3B), indicating complete quenching of photodynamic products. Consistent findings were obtained when the exposure was conducted at 405 nm (Figure S10F, Supporting Information).

Mannitol exhibits a selective scavenging effect on hydroxyl radicals;[29] in this case, if only Type II reaction were to take place, the presence of mannitol should not impact the gain in fluorescence of SOSG. Our results indicate that mannitol only partially mitigates the effect of Ang-Ce6-NLCs under light stimulation (Figure 3C), since some residual fluorescence in SOSG was observed due to the singlet oxygen produced; a similar trend is
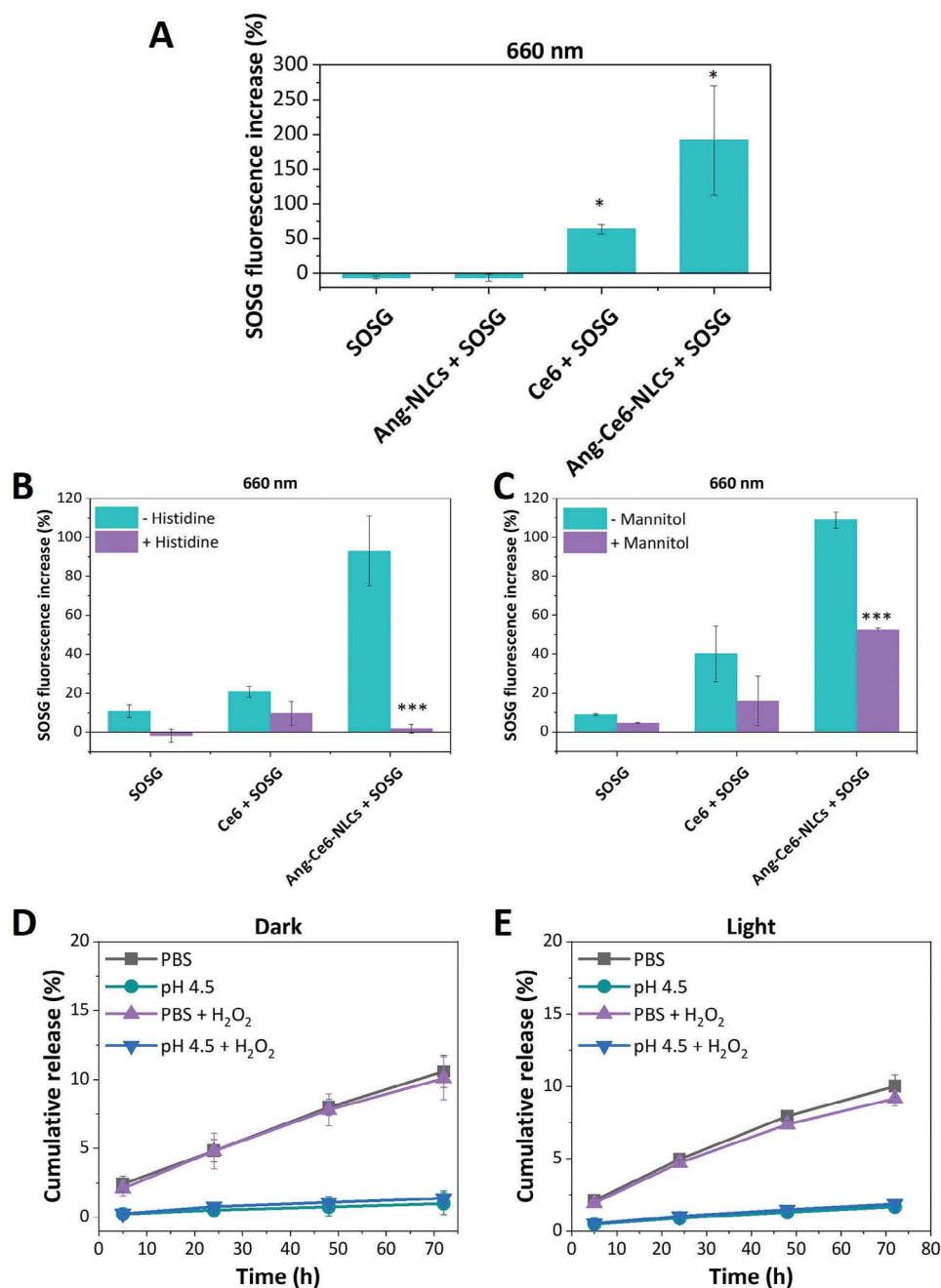
**ADVANCED
SCIENCE NEWS**

www.advancedsciencenews.com

**ADVANCED
HEALTHCARE
MATERIALS**

www.advhealthmat.de

Figure 3. A) Increase of the fluorescence emission of SOSG at 515 nm for different experimental classes. B) Increase of the fluorescence emission of SOSG at 515 nm for different experimental classes, with or without the addition of histidine. C) Increase of the fluorescence emission of SOSG at 515 nm for different experimental classes, with or without the addition of mannitol. D) Cumulative release of Ce6 from Ang-Ce6-NLCs in PBS (gray), pH 4.5 (cyan), PBS + H_2O_2 (violet), pH 4.5 + H_2O_2 (blue). E) Cumulative release of Ce6 from Ang-Ce6-NLCs in PBS (gray), pH 4.5 (cyan), PBS + H_2O_2 (violet), pH 4.5 + H_2O_2 (blue), after light irradiation. (Data are presented as mean ± SD, n = 3, p-values are calculated with one-way ANOVA followed by a Bonferroni post-hoc test, statistical notations without bars refer to the comparison between the experimental classes with the photosensitizers with respect to the probe alone, *$p < 0.05$, **$p < 0.01$, ***$p < 0.001$).

observed with exposure at 405 nm (Figure S10G, Supporting Information).

These experiments collectively suggest that the photodynamic action of Ang-Ce6-NLCs proceeds through both Type I and Type II reactions. Furthermore, it becomes apparent that, as also suggested by other authors, the SOSG probe does not exclusively react with singlet oxygen; rather, other radicals such as hydroxyl radicals may also contribute to its fluorescence enhancement.[30] Thus, caution is warranted when utilizing this probe for the specific detection of this substrate.

**ADVANCED
SCIENCE NEWS**

www.advancedsciencenews.com

**ADVANCED
HEALTHCARE
MATERIALS**

www.advhealthmat.de

The release kinetics of Ce6 from Ang-Ce6-NLCs was assessed by measuring cumulative release over time in various buffers by HPLC analysis, in a suitable mobile phase for Ce6 (i.e., methanol[31]) preventing potential loss of absorption/fluorescence resulting from Ce6 aggregation. As depicted in Figure 3D,E, the release of Ce6 was higher under slightly basic pH (PBS), reaching ≈11 ± 1% after 72 h, due to the enhanced compatibility of Ce6 in such environment, contrasting with the release observed under acidic conditions (1 ± 1%). This trend persisted under mildly oxidative conditions (hydrogen peroxide) or LED stimulation at 660 nm, emphasizing the effective protective role of the nanoparticle core.

While an optimal outcome in tumor therapy would usually entail increased release under acidic pH, given the typically more acidic microenvironment of tumor cells relative to healthy cells, Ang-Ce6-NLCs exhibited the opposite effect. Nonetheless, even at pH 7.4 after 72 h, only ≈10% of the total encapsulated Ce6 was released, indicating significant retention within the nanoparticles. Moreover, as previously shown, Ce6 retains its photodynamic action within Ang-Ce6-NLCs, eliminating the need for extensive release at the target site to elicit anti-tumoral effects. However, an effective targeting of the nanoparticle action to tumor cells remains crucial for maximizing therapeutic efficacy while minimizing adverse effects on healthy cells.

2.4. Ang-Ce6-NLCs Cytocompatibility and Interaction with Cells

The viability of U87 MG cells following treatment with increasing concentrations of free Ce6, empty Ang-NLCs, and Ang-Ce6-NLCs was initially assessed without light stimulation. As illustrated in Figure S11 (Supporting Information), free Ce6 administration did not elicit any discernible variation in cell viability across all tested concentrations, both at 24 and 72 h post-administration. Conversely, treatment with nanoparticles (both Ang-NLCs and Ang-Ce6-NLCs) exhibited a concentration-dependent effect on cell viability. Since concentrations below 500 µg mL^{-1} did not yield statistically significant differences in cell viability, all subsequent experiments were conducted at a safe concentration of 100 µg mL^{-1}.

As already reported,[12] the functionalization of nanoparticles with Ang enhances their targeting capabilities toward GBM by interacting with the low-density lipoprotein receptor-related protein 1 (LRP1), overexpressed on the GBM cell membrane.[10] To evaluate the selective targeting efficacy of Ang-Ce6-NLCs, a custom-designed fluidic bioreactor, schematically represented in Figure S12 (Supporting Information), was employed, allowing for the exposure of various cell lines to a flowing cell medium containing 100 µg mL^{-1} of Ang-Ce6-NLCs, pre-labeled with Vybrant DiO. The selected cell lines for this investigation included primary human astrocytes, brain microendothelial cells (hCMEC/D3), neuron-like cells (differentiated SH-SY5Y), primary human microglia, primary human pericytes, and GBM cells (U87 MG). A higher uptake of Ang-Ce6-NLCs by U87 MG cells compared to Ce6-NLCs was observed (5.7 ± 2.3% vs 2.6 ± 1.1%, $p < 0.05$) as depicted in **Figure** 4. Notably, Ang-Ce6-NLCs exhibited a distinct preference for targeting U87 MG cells over other cell lines ($p < 0.001$), emphasizing the efficacy of Ang in facilitating active targeting of GBM cells. A statistically sig-

nificant increase in Ang-Ce6-NLCs uptake by hCMEC/D3 cells was also noted with respect to Ce6-NLCs (2.1 ± 0.4% vs 1.1 ± 0.3%; $p < 0.01$), consistent with the high expression of LRP1 by brain capillary endothelial cells.[32] These results are in line with previous studies and pave the way for targeting tumor hypervascularization.[33]

Once verified the effectiveness of the targeting, we investigated the uptake and internalization pathways of Ang-Ce6-NLCs in U87 MG cells, following analysis of caveolae- and clathrin-coated vesicles, and pinosomes (Figure S13A–E, Supporting Information). Confocal microscopy elucidated that the nanoparticles are internalized via different pathways. Analysis of Pearson's correlation coefficient indicated that after 6 h of incubation, pinosome-mediated internalization appeared to be the predominant pathway compared to others (0.42 ± 0.02 for pinosomes, 0.21 ± 0.03 for caveolae, and 0.16 ± 0.03 for clathrin). At 24 h, pinosome-associated uptake increased, caveolae-mediated uptake decreased, while clathrin-mediated uptake remained consistent (0.52 ± 0.03 for pinosomes, 0.16 ± 0.02 for caveolae, 0.17 ± 0.03 for clathrin).

To assess the fate of Ang-Ce6-NLCs within U87 MG cells, their co-localization with lysosomes was examined at various time points. Results show that at both 24 and 48 h of incubation, a fraction of Ang-Ce6-NLCs is localized within lysosomes (0.33 ± 0.03 at 24 h, 0.42 ± 0.1 at 48 h), as depicted in Figure S13F,G (Supporting Information).

2.5. Ang-Ce6-NLCs-Mediated PDT: Assessment of Anticancer Efficacy

In vitro light exposures of U87 MG cells, with or without photosensitizer administration, were conducted initially by comparing three LED powers (660 nm; 20, 10, or 2 mW cm^{-2}) for 5 min to determine the optimal stimulation conditions. Cells were first treated with either Ce6 (0.7 µg mL^{-1}) or Ang-Ce6-NLCs (100 µg mL^{-1}, corresponding to 0.7 µg mL^{-1} of Ce6, according to the loading data) for 24 h. Prior to light exposure, the Ang-Ce6-NLCs dispersion or Ce6 solution were replaced with fresh media to exclusively allow the internalized fraction of the photosensitizer to exert its function. As evidenced in **Figure** 5A, the sole light exposure at this wavelength and with these power densities did not affect cell viability. No effect was detected even when cells were pre-treated with Ce6. On the other hand, Ang-Ce6-NLCs exhibited high photodynamic activity at 10 and 20 mW cm^{-2} (44 ± 18% and 1.7 ± 0.9%, respectively). Notably, at a power density of 2 mW cm^{-2}, no substantial impact on cell viability was observed, irrespective of the formulation employed. The higher efficacy of Ang-Ce6-NLCs with respect to free Ce6 may be attributed to the lower capacity of Ce6 in generating ROS under physiological pH conditions due to aggregation phenomena, as already discussed, and/or to a lower internalization rate of the free molecule compared to the nanoparticles. To better understand this behavior, we performed a similar experiment where cells were pre-treated for 24 h with either Ce6 (0.7 µg mL^{-1}) or Ang-Ce6-NLCs (100 µg mL^{-1}), but this time, without medium change before light exposure (20 mW cm^{-2}, 5 min). Figure S14 (Supporting Information) shows that the presence of the photosensitizer during the stimulation significantly impacted the outcome of the cell
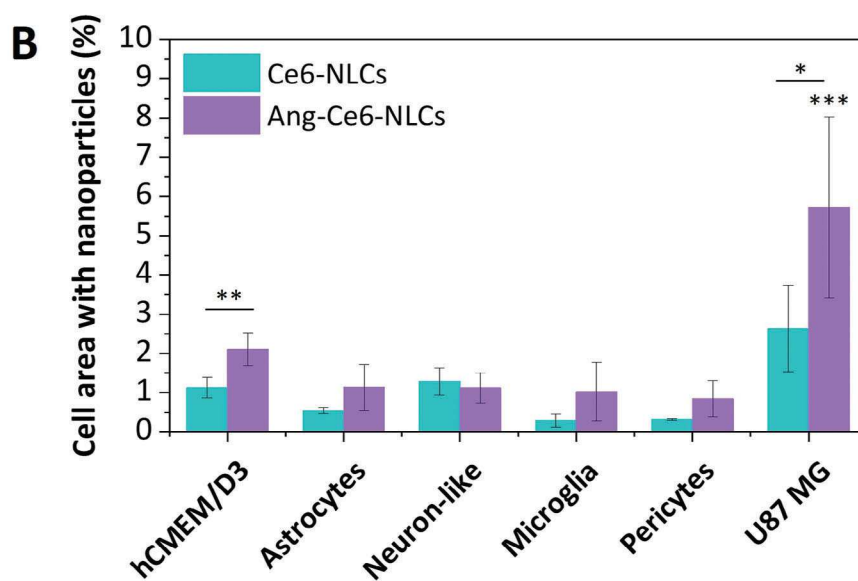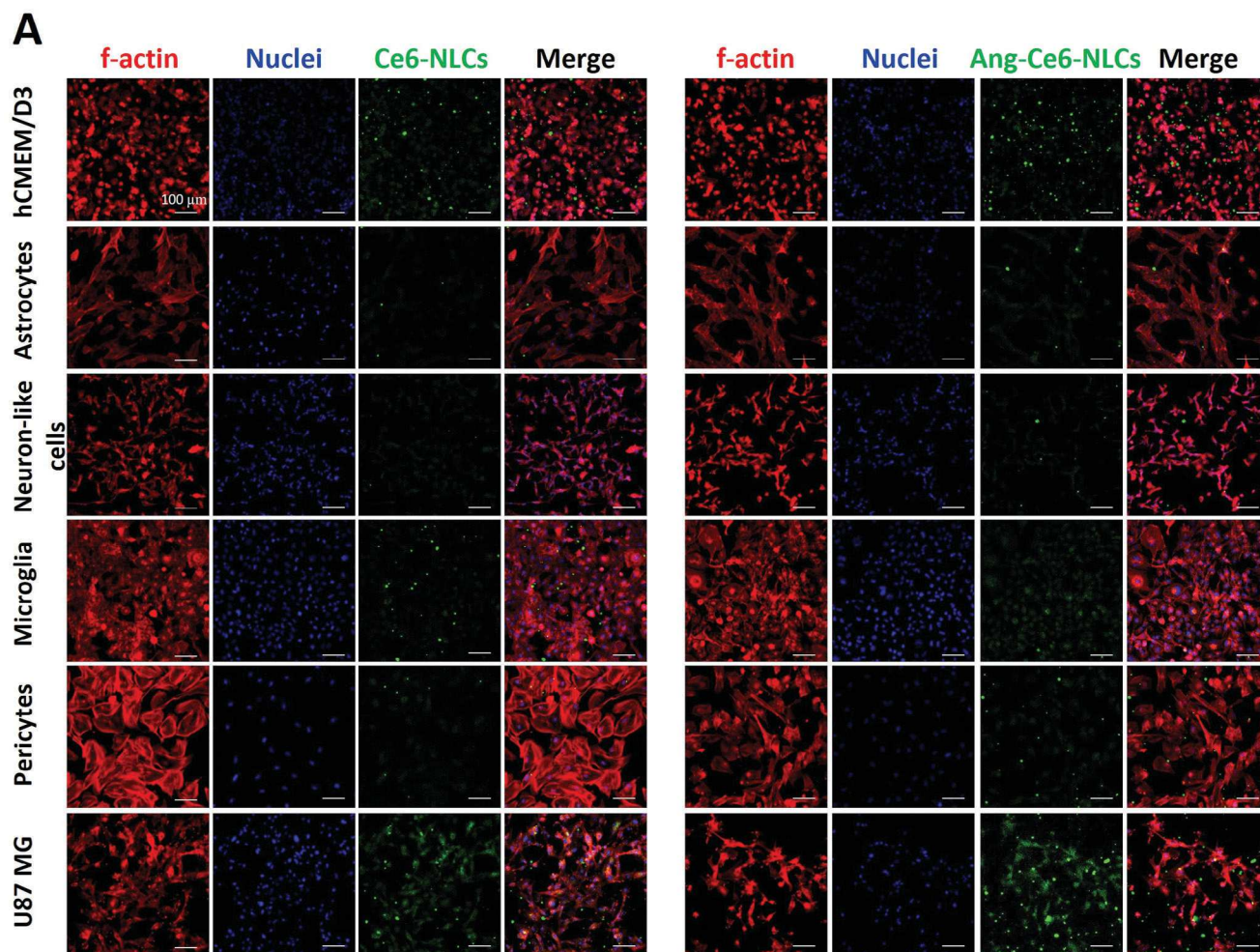
**ADVANCED
SCIENCE NEWS**

www.advancedsciencenews.com

**ADVANCED
HEALTHCARE
MATERIALS**

www.advhealthmat.de

Figure 4. A) Representative confocal images reporting the uptake of Ce6-NLCs and Ang-Ce6-NLCs (in green) by different cell cultures after 3 h of treatment in dynamic conditions. C) Quantitative analysis showing nanoparticles/cells co-localization. (Data are presented as mean ± SD, n = 3, p-values are calculated with one-way ANOVA followed by a Bonferroni post-hoc test, *$p < 0.05$, **$p < 0.01$, ***$p < 0.001$).

**ADVANCED
SCIENCE NEWS**

www.advancedsciencenews.com

**ADVANCED
HEALTHCARE
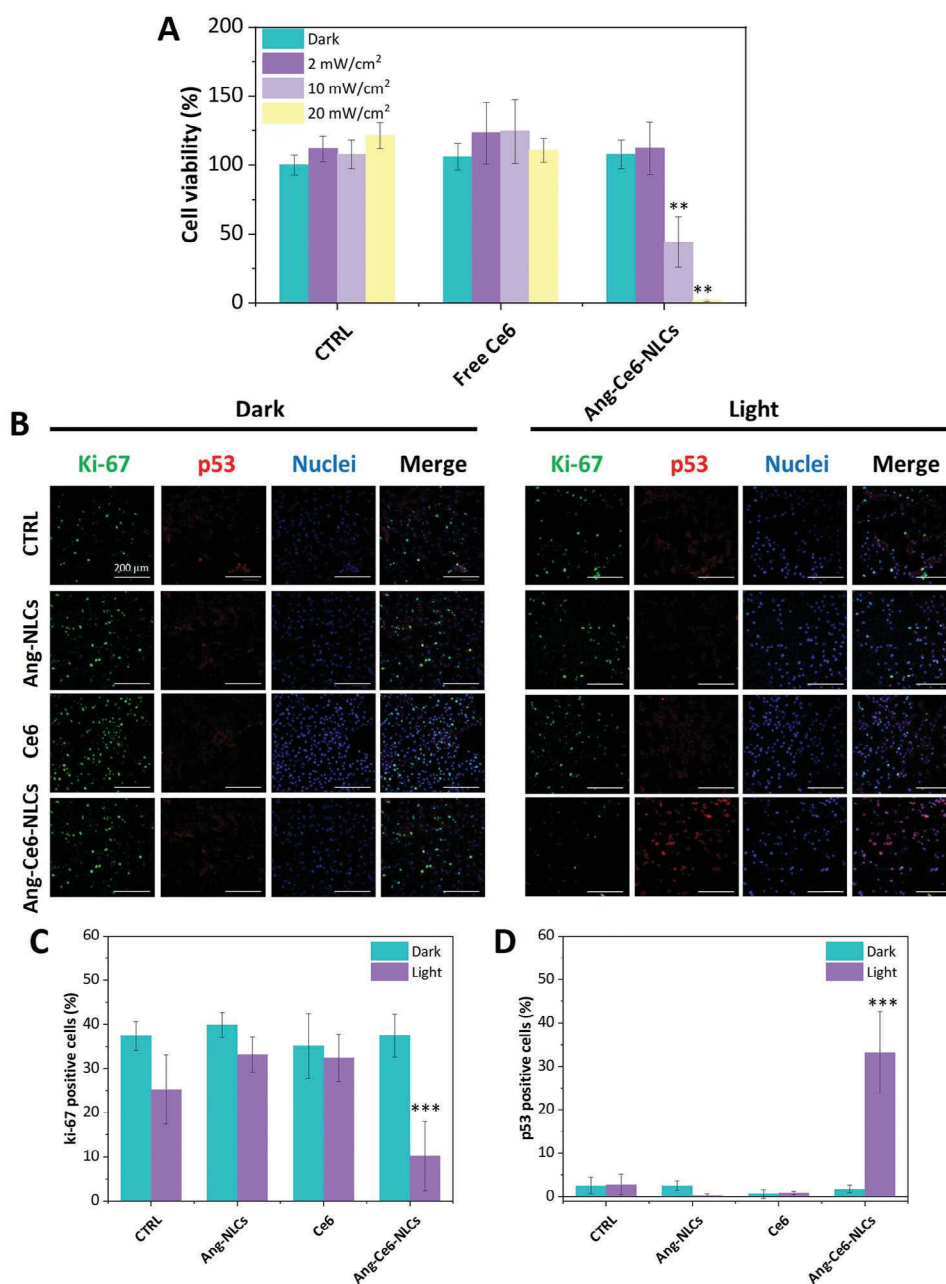MATERIALS**

www.advhealthmat.de

Figure 5. A) Cell viability of U87 MG cells treated with Ce6 or Ang-Ce6-NLCs and irradiated for 5 min with a LED at 660 nm, set at different powers (2, 10, and 20 mW cm^{-2}). B) Representative confocal images reporting p53 (in red) and Ki-67 (in green) expression for all of the experimental classes, with or without light stimulation (660 nm, 10 mW cm^{-2}, 5 min). Quantitative analysis of C) Ki-67 and D) p53 expression. (Data are presented as mean ± SD, n = 3, p-values are calculated with one-way ANOVA followed by a Bonferroni post-hoc test,*$p < 0.05$, **$p < 0.01$, ***$p < 0.001$).

viability, particularly for free Ce6, where a drastic reduction to 9 ± 2% was evidenced. This experiment proves that internalization plays a significant role in PDT, and that the favorable uptake of our Ang-Ce6-NLCs by U87 MG cells enables the reduction of administered photosensitizer concentrations to the target site.

Based on the viability results reported in Figure 5A, a single 5-min treatment at a power density of 10 mW cm^{-2} was chosen as irradiation protocol for all following experiments.

To gain deeper insights into the effects triggered by the treatment, the expression levels of the apoptotic marker p53 and of the proliferative marker Ki67 in U87 MG cells were examined (Figure 5B–D). The considered experimental classes included free Ce6 (0.7 µg mL^{-1}), Ang-NLCs (100 µg mL^{-1}), and Ang-Ce6-NLCs (100 µg mL^{-1}), with or without LED stimulation at 660 nm. Confocal imaging results reveal that only Ang-Ce6-NLCs are capable of inducing apoptosis upon light exposure. Across all the experimental conditions, cells exhibited similar levels of p53 and
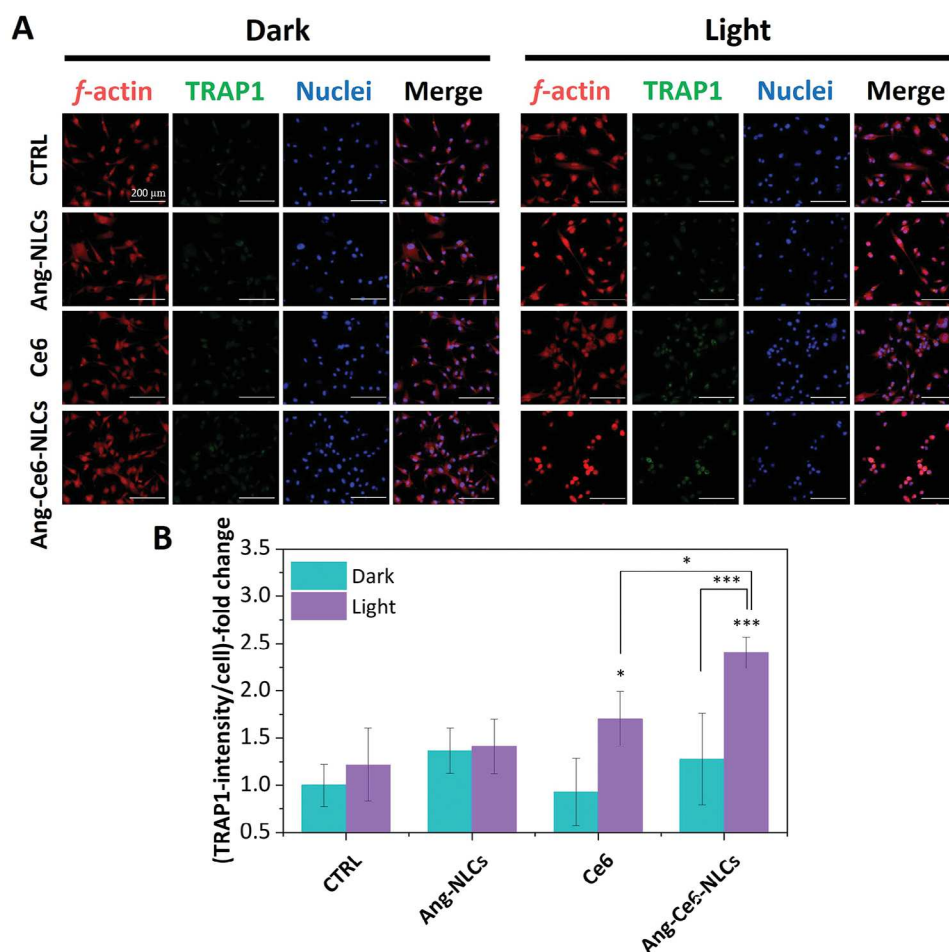
**ADVANCED
SCIENCE NEWS**

www.advancedsciencenews.com

**ADVANCED
HEALTHCARE
MATERIALS**

www.advhealthmat.de

Figure 6. A) Representative confocal images evaluating TRAP1 expression in U87 MG cells undergone different treatments and (B) relative quantitative analysis. (Data are presented as mean ± SD, n = 3, p-values are calculated with one-way ANOVA followed by a Bonferroni post-hoc test, *$p < 0.05$, **$p < 0.01$, ***$p < 0.001$).

Ki67 expression, with the exception of the treatment with Ang-Ce6-NLCs + light, where a statistically significant reduction in Ki67 expression (10 ± 8% vs 37 ± 3% Ki67 positive cells in Ang-Ce6-NLCs + light and untreated control, respectively) and an increase in p53 expression (33 ± 9% vs 3 ± 3% p53 positive cells in Ang-Ce6-NLCs + light and untreated control, respectively) were found. PDT mediated by Ang-Ce6-NLCs thus proves effective in damaging cancer cells, reducing their proliferative potential, and inducing apoptosis.

The production of singlet oxygen and ROS upon light stimulation of photosensitizers is known to induce several intracellular damages and an increase of intracellular oxidative stress, which, in turn, affects cell metabolic activity and, ultimately, triggers cell death. To investigate the impact of Ang-Ce6-NLCs-mediated PDT on oxidative stress, we tracked the expression of TRAP1, a chaperone belonging to the heat shock protein 90 kDa (HSP90) family localized within mitochondria.[34] Numerous experimental findings underscore its pivotal role in regulating mitochondrial dynamics and maintaining its equilibrium during oxidative stress conditions. TRAP1 has been demonstrated to possess antioxidant properties, being thus its expression upregulated following exposure to oxidative stressors.[35] From confocal imaging and the relative analysis reported in **Figure 6**, it is evident that both free Ce6 and Ang-Ce6-NLCs induce upregulation of TRAP1 expression only when combined with light exposure. Moreover, consistently with our previous results, Ang-Ce6-NLCs were more effective in inducing mitochondrial oxidative stress compared to free Ce6 (2.4 ± 0.2 vs 1.7 ± 0.3 -fold change with respect to control cells, $p < 0.05$), again suggesting a pivotal role of the photosensitizer intracellular localization in inducing an effective antitumoral action.

We then explored the efficacy of the proposed treatment in mitigating the migration abilities of GBM cells.[36,37] For this experiment, GBM spheroids were treated for 24 h with either free Ce6, empty Ang-NLCs, or Ang-Ce6-NLCs. Subsequently, the treatment medium was replaced with a fresh one, and spheroids were exposed to light irradiation at 660 nm (10 mW cm⁻², 5 min). Bright-field images of U87 MG spheroids undergoing various treatments are presented in **Figure 7**A,B (images were captured at different post-irradiation time-points: 24, 48, and 72 h), while quantitative analyses are depicted in Figure 7C. Control spheroids continued to grow due to cell proliferation, with cells
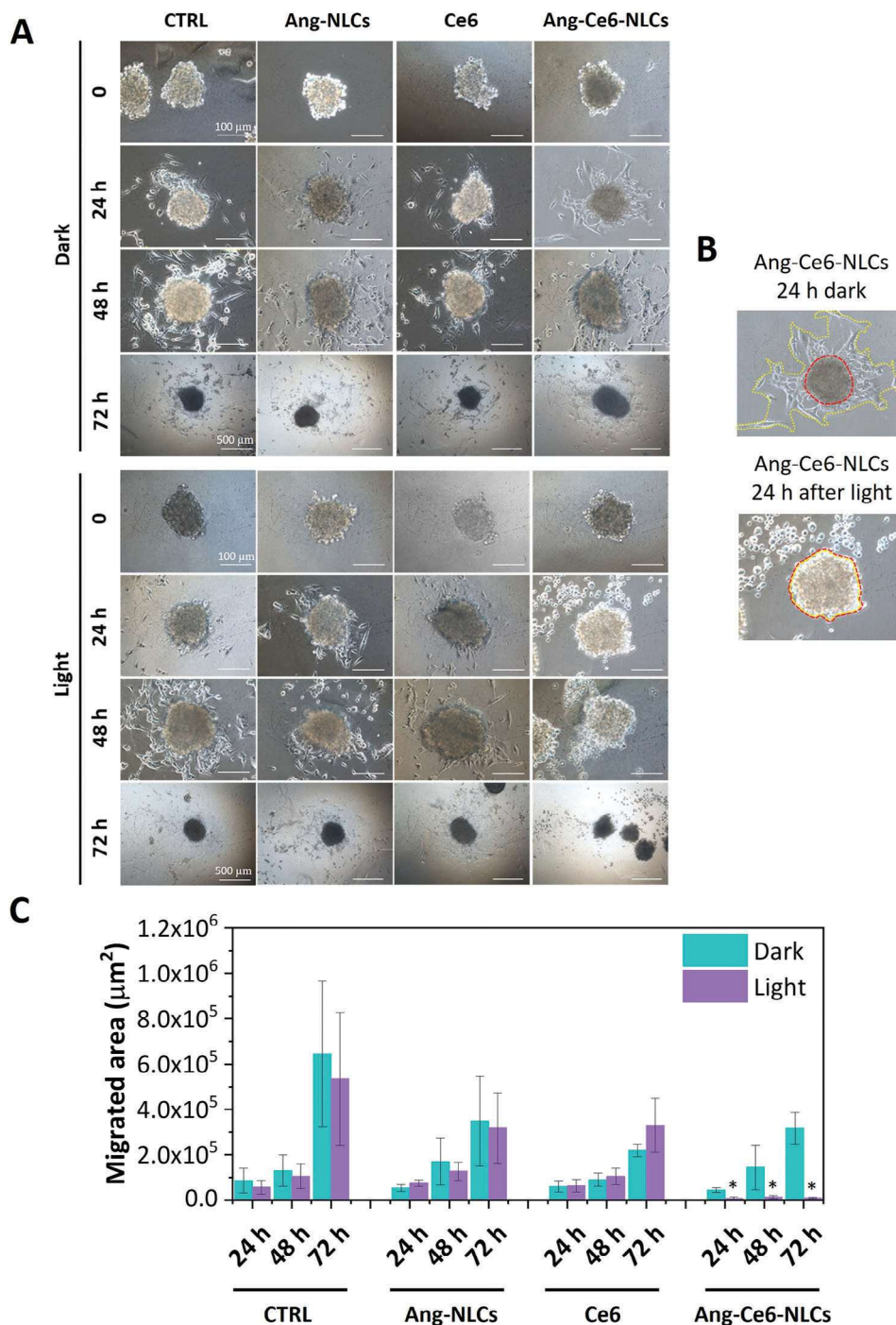
Figure 7. A) Representative optical images of migration tests on U87 MG spheroids. B) Further examples of spheroids treated with Ang-Ce6-NLCs and irradiated with light after 24 h. The yellow line marks the migration border, while the red line highlights the spheroid core. C) Quantitative analysis of the migration area. (Data are presented as mean ± SD, n = 6, p-values are calculated with Kruskal–Wallis ANOVA, *$p < 0.05$).

migrating from the surface toward other adhesion sites, regardless of the stimulation with light. A similar trend was observed in spheroids treated with free Ce6 and empty Ang-NLCs (with or without light stimulation), or in Ang-Ce6-NLCs without light irradiation. Just when Ang-Ce6-NLCs were combined with light stimulation, no significant migration increase could be observed

24 h post-treatment, as the spheroids failed to adhere to the surface of the well. Moreover, no subsequent recovery of migration abilities was observed over longer times, even without further exposing the spheroids to PDT (Figure 7B,C). These results underscore the effectiveness of PDT mediated by Ang-Ce6-NLCs in inhibiting cell migration. Moreover, since just one stimulation

Table 3. Experimental design for proteomics. Forty samples were utilized to define three sub-studies, investigating the effects of photodynamic treatment (or some of its components) and/or culture passages on cell proteomes. The second batch (class 2, samples A2, B2, C2, D2, E2, F2, G2, H2) was eventually regarded as an outlier and discarded.

	α (main study – effects of treatment, at all time-points), $n = 5$		
Proteomics sub-study	Class identifier	Description	Replicas
	A	untreated	A1, A2, A3, A4, A5
	B	Ce6	B1, B2, B3, B4, B5
	C	Ang-NLCs	C1, C2, C3, C4, C5
	D	Ang-Ce6-NLCs	D1, D2, D3, D4, D5
	E	Light	E1, E2, E3, E4, E5
	F	Ce6 + light	F1, F2, F3, F4, F5
	G	Ang-NLCs + light	G1, G2, G3, G4, G5
	H	Ang-Ce6-NLCs + light	H1, H2, H3, H4, H5
	β (effects of treatment, on selected samples at a single time point), $n = 2$		
Sub-study	Class identifier	Description	Replicas
	Ax	untreated	A4, A5
	Dx	Ang-Ce6-NLCs	D4, D5
	Fx	Ce6 + light	F4, F5
	Hx	Ang-Ce6-NLCs	H4, H5
	γ (effects of culture passage), $n = 8$		
Sub-study	Class identifier	Description	Replicas
	1	frozen at day 0	A1, B1, C1, D1, E1, F1, G1, H1
	2	frozen at day 6	A2, B2, C2, D2, E2, F2, G2, H2
	3	frozen at day 22	A3, B3, C3, D3, E3, F3, G3, H3
	4	frozen at day 54	A4, B4, C4, D4, E4, F4, G4, H4
	5	frozen at day 54	A5, B5, C5, D5, E5, F5, G5, H5

session already provided a significant effect, the promising potential of the proposed procedure is highlighted, in particular for direct integration into future surgical resection procedures. In such scenario, nanoparticles could be administered to the tumor site during surgery and safely stimulated, offering a suitable approach to hinder tumor cell migration after the surgical resection.

2.6. Proteomics

The spheroids collected in all experimental replicates had an average diameter of 170 µm, and were obtained from 10.8×10^3 cell seeding in each well, except for batch 2 where the spheroids had an unusually larger diameter, ≈450 µm average diameter obtained from 27.2×10^3 cells for each well. All proteomics classes, nomenclature, sub-studies, and replicas considered in this work are summarized in **Table 3** and Table S2 (Supporting Information).

Principal component analysis (PCA) correctly identifies the 5 different experimental batches as four clusters. Batches 4 and 5, frozen at the same time point, fall in a common area. Excepting batch 2, time points are spatially organized in a temporally coherent order along component 1. Each cluster seems to recapitulate a common architecture in terms of experimental classes, which appear to be arranged in somewhat stereotyped modalities. This is perhaps less evident for replica 2, becoming in turn obvious within the region of batches 4 and 5, where couples of samples belonging to a given class are close to

each other. Such results are presented in Figure S15 (Supporting Information).

A hierarchical clustering (HC) of all proteins and samples of the proteomics dataset classifies samples based on the temporal replica they belong to, confirming culturing time as the prevalent variable. In line with PCA, batch 2 is identified as an outgroup (Figure S16, Supporting Information). When carried out on sub-study β only (**Figure 8A**), the procedure has still enough resolution to group samples according to the class of origin. Class Hx – the one receiving a full nanotechnological PDT – forms an outgroup. The other branch of the dendrogram organizes classes Dx and Fx, respectively Ce6 within NLCs or free-standing Ce6 plus light, as closer to each other, with respect to class Ax, our untreated control.

Venn and gene ontology (GO) analyses on sub-studies α and γ also suggest a comparatively stronger impact of culture passage on cell proteome, compared to treatment (Figure S17, Supporting Information). Still, sub-study β retains sufficient information to spot at least some of the putative molecular drivers of PDT, in terms of both proteins and GO terms associated with them.

Sub-study α only produces differentially represented proteins (DRPs) in numbers greater than 1 for 4 of its comparisons, namely three of those exploring photodynamic effects and involving class H (H-A, 59 DRPs; H-B, 52 DRPs; H-E, 26 DRPs), plus D-A (7 DRPs), investigating basal nanoparticle toxicity. On the four-way Venn diagram that can be obtained from such parent sets, the intersection H-A, H-B, and H-E is the one that bears the most potential in terms of candidate mediators of the
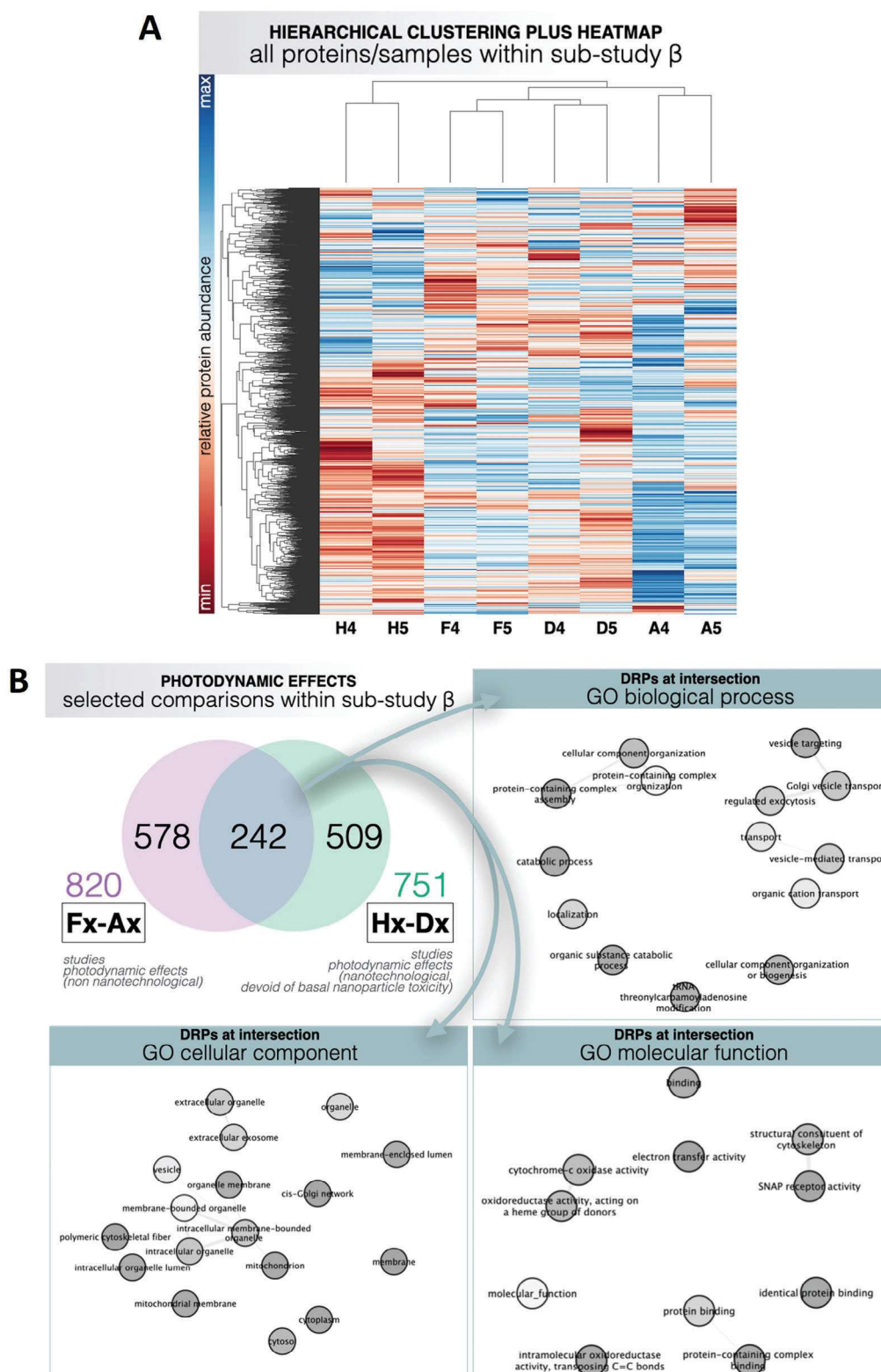
Figure 8. A) HC reflecting similarities across all proteins and samples within proteomics sub-study β. In the central heatmap, each row is dedicated to a single protein, and each column is devoted to a different sample. Relative protein abundances (RPAs) are represented as colors on individual cells. n = 2. RPA variations were statistically evaluated through significance B tests, with a significance cutoff for q-values from Benjamini-Hochberg false discovery rates (FDRs) set to 0.05. max = maximum; min = minimum. B). Proteins responding to photodynamic treatment, irrespective of formulation (nanotechnological or non-nanotechnological) and in the absence of variations in the culture passage, as identified by a Venn diagram featuring two

**ADVANCED
SCIENCE NEWS**

www.advancedsciencenews.com

**ADVANCED
HEALTHCARE
MATERIALS**

www.advhealthmat.de

therapeutic effects of photodynamic treatment. With 8 proteins, all consistent, such a sub-set is also the richest in terms of proteins. Sub-study γ yields a plethora of DRPs and a diverse array of GO terms for those comparisons studying passage effects, that is 3-1 (early passages, 1437 DRPs) and 4-3 (late passages, 1851 DRPs). At their intersection, 568 DRPs are found, all consistent. Comparison 5-4, a negative control, comprises no DRPs.

At the intersection between Fx-Ax and Hx-Dx, studying photodynamic effects respectively through non-nanotechnological or nanotechnological means, 242 DRPs are found, roughly 1/3 of those found at each parent set. GO analyses on these return terms generally pertaining vesicular transport and oxidoreductions (Figure 8B).

To sum up, culture passage appears to be a major driver of protein alterations. Still, after careful analysis, treatment-associated effects are recognizable, and these seem to support the existence of adaptations to redox imbalance specifically for PDT-receiving cells.

2.7. Evaluation of the Effects of Ang-Ce6-NLCs-Mediated PDT in a Fluidic Neurovascular Unit Model

Using LEDs for PDT offers several advantages over lasers, including lower costs, reduced risks, and the ability to treat larger tumor areas in less time. Our results indicate that by enhancing Ce6 intracellular localization through GBM-targeted nanoparticles, effective anti-tumoral effects can be achieved at lower power densities, potentially obviating the need for lasers. However, irradiating larger areas with LEDs raises concerns about potential harmful effects on healthy cells. Preserving the delicate brain environment is critical for patient well-being. The proposed targeting strategy, employing Ang on nanoparticle surface, facilitates preferential internalization by GBM cells, thereby enhancing PDT effects in tumor cells. Thus, higher PDT effects are expected in tumor cells due to a higher accumulation of the photosensitizer. Yet, it is crucial to assess treatment effects on healthy cells, ideally using models that mimic clinical settings, where not only tumor cells are exposed to the treatment. Studying this effect directly in vivo could be challenging, as tumor xenograft or genetically engineered mouse models lack reproducibility in brain cancer studies.[38] Furthermore, in the aim of understanding the outcome of the treatment on different components of the NVU, we need to separate each component to individually study effects not only on the target cells, but also on all the neighboring healthy cells. Acquiring this kind of information is particularly important and yet often difficult to obtain in vivo. Therefore, the use of appropriate in vitro models becomes essential for a comprehensive evaluation of treatment outcomes on different cell types.

In this work, we developed a fluidic model of the human brain cancer microenvironment (**Figure 9A**; Figure S18, Supporting Information). The size of the bioreactor was designed to fit the irradiation set-up and, was integrated to host a temperature detector for real-time monitoring of the temperature during irradiation and electrodes for trans-epithelial electrical resistance (TEER) measurement (Figure S19, Supporting Information). The bioreactor is composed of a fluidic channel on the top part simulating brain capillaries, with brain endothelial cells, astrocytes, and pericytes forming a BBB model, and a lower chamber representing the brain compartment – populated with healthy cells; neurons, microglia, astrocytes – but also populated with a GBM model. Although our primary focus was not on nanoparticle passage through the BBB, as their potential intraoperative administration would be more pertinent, maintaining proper flow in the BBB model is crucial to develop a realistic BBB phenotype, recapitulating physiological conditions and assessing the effects of PDT on the whole brain cancer environment. Angiopep-2 in Ang-Ce6-NLCs, for example, binds to the LRP1 receptor, extensively expressed by brain endothelial cells, suggesting its relevance in the interactions with the BBB. Studies indicate that low-density lipoprotein receptor expression may increase with appropriate shear stress,[39] emphasizing the importance of flow for understanding Ang-Ce6-NLCs interactions with the BBB model.

To assess the actual shear stress experienced by the BBB model in the fluidic channel of the bioreactor at different flow rates, we conducted fluid dynamic FEM numerical simulations using COMSOL Multiphysics software. These simulations evaluated velocity spatial distributions at different inlet flow rates inside the bioreactor chamber, maintaining a fixed channel height (h) of 0.5 mm. Adopting the laminar flow interface, which accounts for stationary and laminar flow conditions via simplified Navier–Stokes equations, the Reynolds number (Re) was calculated from Equation 11 (Experimental Section) to be 81.2 for $Q_i = 12$ mL min$^{-1} = 2 \times 10^{-7}$ m^3 s^{-1}, considering $D_H = 9.1 \times 10^{-4}$ and < $v \geq 0.08$ m s^1, indicating laminar flow behavior. Figure S20A (Supporting Information) shows the geometrical model and the boundary conditions used in the simulation, mimicking the actual geometry of the channel. 3D color maps in Figure S20B (Supporting Information) represent the spatial velocity field distribution within the flow chamber, demonstrating a parabolic velocity trend along the z-direction. Additionally, a 2D color map illustrates the velocity distribution on the cross-section of the duct (zx-plane), indicating maximum velocity at the center (Figure S20C, Supporting Information; twice the average velocity in the pipe).[40,74,75] Figure S20D (Supporting Information) represents the color map of shear stress distribution along the x-direction (τ_{xz}) on the bottom surface of the bioreactor flow chamber, for an inlet flow rate $Q_i = 12$ mL min^{-1}. As indicated by the color scale, in the long linear path of the duct, far from the inlet, the outlet, and the corners, the wall shear stress has a value of ± 0.85 N m^{-2}. Naturally, in the proximity of the inlet and the outlet, where the flowing direction is along y-axes, the τ_{xz} values are zero, while the shear stress along the y-direction

---

pairwise comparisons picked up from proteomics sub-study β. The number of proteins found within all parental sets and subsets are reported. GO analyses for all DRPs at the intersection yield significantly enriched GO terms for GO biological function, GO cellular component, and GO molecular function. GO scatter plots display each term on a grey circle, the color saturation of which positively correlates with statistical support (darker shades for lower p-values). Gray lines connect semantically similar GO terms. Such lines become broader when such resemblances are strong. Terms are also roughly mapped to reflect analogies in meaning, but their exact positions were adjusted whenever needed for graphical purposes.
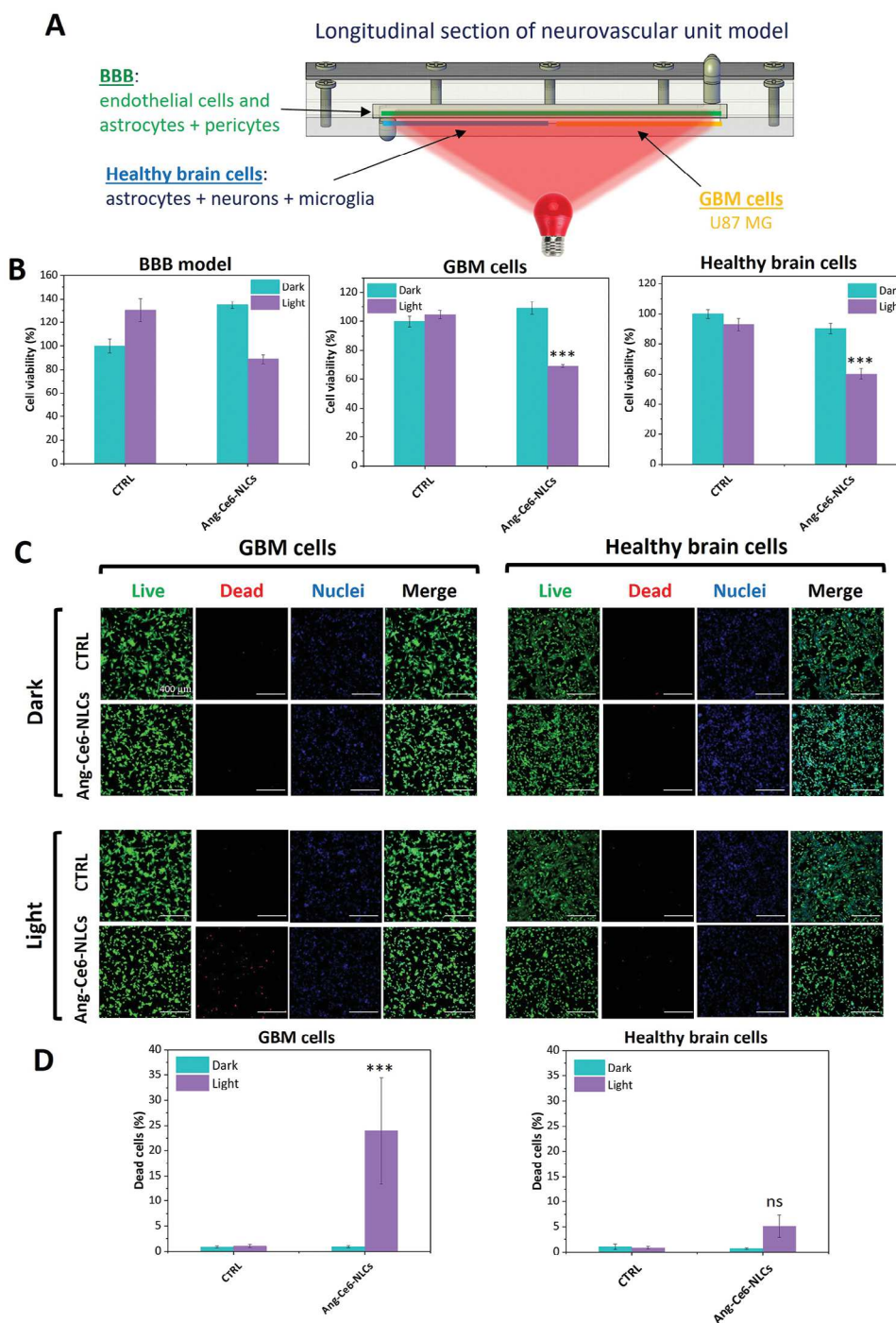
Figure 9. A) Schematic longitudinal section of the bioreactor during a typical LED irradiation experiment. B) Viability of the components of the NVU model (BBB, U87 MG cells, and healthy brain cells) in different conditions. C) Representative images of the Live/Dead assay on the U87 MG and healthy cells following different treatments and D) quantitative analysis. (Data are presented as mean ± SD, n = 3, p-values are calculated with one-way ANOVA followed by a Bonferroni post-hoc test, *p < 0.05, **p < 0.01, ***p < 0.001, ns = not significant).

(τ_{yz}) dominates, reaching values comparable to τ_{xz} (Figure S20E, Supporting Information). The shear stress locally increases at the corners of the flow chamber, where the flow path is perturbed, reaching maximum values. Figure S20F (Supporting Information) shows the plot of the maximum value of shear stress with respect to the inlet flow rate. At the maximum simulated flow condition ($Q_i = 12$ mL $= 2 \times 10^{-7}$ m³ s⁻¹), the shear stress at the corners reaches 2 N m⁻². Based on this simulation, a flow rate of 12 mL min⁻¹ allows us to reproduce the typical shear stress experienced by brain capillaries (1–2.3 N m⁻²).[41,42]

The formation of a tight BBB model was demonstrated by confocal microscopy (Figure S21A, Supporting Information). The cells appear at total confluence, without holes or gaps, with packed morphology. Furthermore, the immunoassay for zonula occludens-1 (ZO-1) showed the presence of this marker, the indication of a mature endothelium (Figure S21A,B, Supporting Information). Another interesting finding is the mutual interaction between endothelial cells of the upper layer and the closely connected pericyte and astrocyte cells of the lower layer. As reported in Figure S21 (Supporting Information), the three cell populations formed a single complex and stable barrier, as also suggested by the expression of ZO-1 and by the measured TEER of 200 ± 30 Ω cm^2, in line with the values reported in the literature.[43]

After the formation of a mature BBB, the bottom chamber was populated with a co-culture of primary human astrocytes, human neuron-like cells (differentiated SH-SY5Y cells), and primary human microglia, alongside GBM cells. A dispersion of 100 µg mL^{-1} of Ang-Ce6-NLCs was administered in the bottom chamber and after 24 h replaced with fresh media. The bioreactor was subsequently exposed to light within the irradiation set-up (**Figure 9**A; Figure S22, Supporting Information). No significant increment of temperature was detected throughout the duration of the stimulation. After the stimulation, the TEER was again measured, showing no differences with respect to the value observed before the experiment. Then, the NVU bioreactor was disassembled and the components, including the BBB model, healthy brain cells, and GBM cells were collected and analyzed separately to understand the effect of PDT within each compartment. As evidenced by Figure 9B, the viability of the BBB model was not significantly affected by the combined treatment of Ang-Ce6-NLCs + light (89 ± 3% viability); on the other hand, a reduction in the metabolic activity of GBM cells and of healthy brain cells was observed (69.1 ± 0.9% and 60 ± 4%, respectively). A reduction in viability from this assay might be the result of the reduction in cell number due to cell death and/or to a decrease in cells metabolic activity following the treatment. To discriminate between these two situations in the cell types that experienced a reduction of viability after PDT (i.e., healthy brain cells and GBM cells) and to understand if this effect on cell metabolism was translated into an induction of cell death, a live/dead assay was performed (Figure 9C,D). Differently from the WST-1 assay (see Experimental Section) used to monitor cell viability, the live/dead assay can highlight the presence of dead cells, since one of the two dyes, namely ethidium homodimer-1, is normally cell impermeable; thus, it can enter cells only when their membrane is damaged. The live/dead assay showed a significant increase of dead cells only in GBM cells (24 ± 11% of dead cells), while a non-significant amount of dead cells (5 ± 2%) was found in the healthy cultures. These results show that in GBM cells the PDT treatment led to a consistent decrease in cell viability, corresponding to an increase in dead cells, suggesting that the lower viability might be ascribed to cell death following PDT. On the other hand, in healthy cells, the decrease in cell viability does not correspond to an increase of dead cells, thus suggesting that in this case, the ROS produced during PDT might mainly influence the cellular metabolism; in fact, being ROS normally involved in cell metabolic pathways, a different concentration induced by PDT might slightly impact cellular homeostasis. Nevertheless, thanks

to the higher accumulation of the nanoparticles in GBM cells for the targeting action of Ang, it is most likely that the concentration of ROS produced in healthy cells is not high enough to trigger cell death. This experiment suggests that the combination of Ang-Ce6-NLCs with light stimulation at 660 nm is an effective procedure for intraoperative GBM treatment. This approach demonstrates an apoptotic effect on GBM cells facilitated by the enhanced uptake provided by the targeting moiety Ang. Importantly, it induces a minimal impact on the metabolic activity of adjacent healthy brain cells, which does not translate into cellular death, suggesting limited side effects.

3. Conclusion

This study introduces a novel approach to PDT for treating GBM using Ce6 encapsulated in nanostructured lipid carriers (Ang-Ce6-NLCs) and targeted with the Ang peptide. By employing low-power LED irradiation at 660 nm, the treatment demonstrates effective anti-tumor action against GBM cells while minimizing potential safety concerns associated with high-power lasers. The efficient PDT effect triggered by Ang-Ce6-NLCs even after only a single 5-min stimulation with LED light paves the way for a new intraoperative treatment of GBM, exploiting a tumor-targeted solution, with potentially lower side effects for the patient.

4. Experimental Section

Nanoparticle Synthesis: Nanostructured lipid carriers loaded with Ce6 (Ce6-NLCs) were produced by the hot sonication method. Precisely, 2.5 mg of oleic acid (Sigma–Aldrich), 27.5 mg of cetyl palmitate (Gattefossé SAS), 3 mg of 1,2-distearoyl-*sn*-glycero-3-phosphoethanolamine-poly(ethylene glycol) (DSPE-PEG) (5000 Da, Nanocs, Inc) and 1 mg of 1,2-distearoyl-*sn*-glycero-3-phosphoethanolamine-N-[succinimidyl(polyethylene glycol)] (DSPE-PEG-NHS) (5000 Da, Nanocs, Inc), were combined with 1 mg of Ce6 (Sigma–Aldrich) in 100 µL ethanol. This mixture was heated at 70 °C to melt lipids and allow the evaporation of ethanol. Then, 3 mL of a 1% w/w aqueous solution of Pluronic F127 (Sigma–Aldrich), also heated at 70 °C, was added to the lipid mixture; finally, the emulsion was sonicated with an ultrasonic tip (Fisherbrand Q125 Sonicator) for 10 min at 90% amplitude. Vials were then stored at 4 °C for 30 min. To prepare empty NLCs, the same procedure was followed without adding Ce6 to the lipid mixture. Both NLCs and Ce6-NLCs were purified using an Amicon centrifuge filter (Ultra-4 Centrifugal Filter Unit, 100 kDa) at 4470 *g*, 15 °C for 40 min, repeating this step three times. After each centrifuge cycle, the filtered solution was removed, and the pellet was re-suspended in MilliQ water. After the last centrifugation step, the remaining pellet was re-dispersed in 4 mL of MilliQ water and stored at 4 °C. The concentration of NLCs and C6-NLCs was determined by freeze-drying a known amount of the dispersion.

Nanoparticle Functionalization: In order to functionalize NLCs and Ce6-NLCs with Ang (Selleckchem), 200 µL of an Ang solution in water (1 mg mL^{-1}) were added to the Ce6-NLC or NLC dispersion to have an approximate theoretical DSPE-PEG-NHS:Ang molar ratio of 1:2, as previously reported.[12] The dispersion was diluted in phosphate-buffered saline solution (PBS, Sigma–Aldrich), to optimize the pH for the reaction between N-hydroxysuccinimide (NHS) and the amine groups on the peptide, and then left under gentle shaking for 4 h in ice. In the end, the solution was washed three times by centrifugation (4470 *g*, 40 min, 14 °C) with Amicon centrifuge filter (Ultra-4 Centrifugal Filter Unit, 100 kDa), and the final pellet was re-dispersed in 4 mL of MilliQ water to obtain either Ang-Ce6-NLCs or plain Ang-functionalized NLCs (Ang-NLCs).

For confocal imaging, Ang-Ce6-NLCs and Ce6-NLCs were labeled with the fluorescent dye Vybrant DiO (Invitrogen) by incubation of 1 mg of

nanoparticles with 10 µL of Vybrant DiO for 2 h at 37 °C. Then, labeled nanoparticles were washed three times by centrifugation (4470 g, 40 min, 14 °C) with an Amicon centrifuge filter (Ultra-4 Centrifugal Filter Unit, 100 kDa), and finally re-dispersed in MilliQ water.

Nanoparticle Characterization: TEM was used to inspect the morphology and size of the nanoparticles. Prior to measurement, samples were diluted in water to a final concentration of 100 µg mL^{-1} and underwent sonication for 2 min. For each sample, a droplet was placed onto a copper grid (150 mesh) coated with an ultrathin amorphous carbon film. After 20 s, the excess droplet was removed using filter paper, and the grid was rinsed with Milli-Q water. Subsequently, a drop of a 1% uranyl acetate solution in water was applied to the grid for 60 s to stain the sample. Finally, the excess solution was removed with filter paper, and images were captured using a JEOL Jem-1011 electron microscope operating at 100 kV with a single-tilt sample holder.

DLS measurements were conducted using a Zetasizer NanoZS90 (Malvern Instruments Ltd) to determine the hydrodynamic diameter and the ζ-potential of Ce6-NLCs and Ang-Ce6-NLCs at 37 °C. A 100 µg mL^{-1} dispersion of the nanoparticles in water underwent sonication for 30 s using a Bandelin ultrasonic probe (8 W) prior to measurement. The stability of Ang-Ce6-NLCs was assessed at pH 4.5 (0.05 M phosphate buffer, to mimic the acidic tumor microenvironment and/or acidic organelles), pH 4.5 + 100 µM hydrogen peroxide (to mimic the higher concentration of hydrogen peroxide in the tumor microenvironment[15]), pH 7.4 (PBS, physiological pH), pH 7.4 + 100 µM hydrogen peroxide, DMEM (Euroclone) supplemented with 10% FBS (DMEM + FBS), and DMEM + FBS + 100 µM hydrogen peroxide. The stock dispersion of the nanoparticles was diluted to a final concentration of 100 µg mL^{-1} in the respective dispersion solution. The hydrodynamic diameter was measured at various time intervals up to 30 days (endpoint). The intensity distribution was determined via CONTIN analysis from the correlogram, while the hydrodynamic diameter and polydispersity index were obtained through cumulant analysis.

SDS-PAGE was conducted to confirm the successful functionalization of the nanoparticles with the peptide. Each sample (37.5 µL of Ang, Ce6-NLCs, or Ang-Ce6-NLCs at a known concentration was mixed with 12.5 µL Laemmli buffer (BioRad) and heated at 95 °C for 10 min. A 4–15% Mini PROTEAN TGX Precast Protein Gel (BioRad) was inserted into an electrophoresis cell (Mini-PROTEAN Tetra Cell, BioRad) filled with Tris/Glycine running buffer (BioRad); then, 50 µL of the sample were loaded into each well; one well was loaded with a molecular weight marker (PageRuler Plus Prestained Protein Ladder, Thermo Fisher Scientific). The gel was then run at 100 V for 1 h. Subsequently, the gel was stained with Coomassie Blue solution (0.125 g brilliant blue R250, 10 mL glacial acetic acid, 40 mL water, 50 mL methanol) for 1 h under gentle agitation. After staining, the gel underwent two rinses with a de-staining solution (10% glacial acetic acid, 40% water, 50% methanol) for 20 min. Finally, the gel was washed with sterile distilled water.

Ang-Ce6-NLCs optical properties were studied with UV/visible and fluorescence spectroscopy, and compared to those of free Ce6 in different conditions, namely MilliQ water, pH 4.5, PBS, and DMEM + FBS. The absorbance spectra of Ang-Ce6-NLCs and Ce6 were evaluated with a UV/visible spectrophotometer (PerkinElmer, Lambda45). Disposable PS cuvettes were used for analysis in the wavelength range of 300–800 nm. Fluorescence spectroscopy was performed with a fluorescence spectrofluorometer (Agilent Technologies, Cary Eclipse) to evaluate fluorescence emission between 415 and 800 nm after excitation at 405 nm.

Ce6 loading in Ang-Ce6-NLCs was quantified with fluorescence spectroscopy (Agilent Technologies, Cary Eclipse). A known amount of Ang-Ce6-NLCs were diluted 1:600 in DMSO, to allow the dissolution of the nanoparticles. The emission of Ce6 in DMSO at 673 nm after excitation at 405 nm was measured to determine the concentration, using a calibration curve obtained by measuring different Ce6 solutions in DMSO. Ce6 loading (%) and encapsulation efficiency (EE) were calculated using Equations (1) and (2):

$$Ce6 \ loading \ (\%) = \frac{Ce6 \ in \ Ang-Ce6-NLCs \ (mg)}{Total \ mass \ of \ Ang-Ce-NLCs \ (mg)} \times 100 \quad (1)$$

$$EE \ (\%) = \frac{Ce6 \ loaded \ in \ Ang-Ce6-NLCs \ (mg)}{Initial \ Ce6 \ in \ the \ formulation \ mixture \ (mg)} \times 100 \quad (2)$$

In order to validate the Ce6 loading obtained with this method, the same was also quantified by HPLC with a Shimadzu LC-20AT, using a C-18 column (150 mm × 4.6 mm i.d., 5 µm particle size). Freeze-dried Ang-Ce6-NLCs (1 mg) were dissolved in 400 µL of methanol and heated at 70 °C for 1 h to melt the lipid core. The sample was centrifuged at 16 000 g for 90 min at 4 °C, and the supernatant was collected and measured with HPLC. The mobile phase was composed of 80% methanol (for HPLC, ≥99.9%, Sigma–Aldrich) and 20% water (HPLC Plus, Sigma–Aldrich), pumped in isocratic mode at a flow rate of 1 mL min^{-1}. The peak of Ce6 was found at a retention time of 7 min, and its intensity was monitored by a UV detector at 405 nm.

LED Stimulation Set-Up: The custom illuminator for multi-well culture plates consists of a control module and a sample holder manufactured via 3D printing (Form3B, FORMLABS) in Grey Pro Resin in the lab. Both the sample holder and the LED board (base: 10 × 16 cm; total height sample holder plus protective cover: 11 cm; height of the sample holder: 7.5 cm) were designed to ensure even illumination across the two central rows of a 24-well plate. Optical excitation was provided by a LED system, the duty cycle, repetition rate, and intensity of which were set through a custom-made control circuit, comprising a microcontroller, a digital-to-analog converter, and an analog LED driver connected to 7 red LEDs (XPGDPR-L1-0000-00F01; Cree, Inc., Durham, NC) with a maximum emission wavelength of 660 nm. The central row of LEDs can be replaced with LEDs operating at other wavelengths (e.g., 405 nm). This set-up enables simultaneous irradiation of 12 central wells of a 24-well plate with a uniform power density ranging from 1 to 25 mW cm^{-2}. The radiant intensity at the level of a multi-well bottom was measured with a calibrated silicon photodiode (S1337-66BR, Hamamatsu), as reported previously.[44]

Numerical simulation of light diffusion from the light sources to the 24-well cell culture plate was performed through FEM in COMSOL Multiphysics to evaluate the actual intensity of light on cell cultures. Light propagation through absorbing or scattering media can be described through the radiative transport equation, which quantifies energy within a volume element as light traverses scattering/absorbing media.[45] The radiative transport equation is complex and depends on several variables; thus, a simplified version, i.e., the diffusion equation (DE), is commonly employed.[46] The light DE is given by Equation (3):[45]

$$\frac{1}{c}\frac{\partial \Phi(r,t)}{\partial t} - D\nabla^2\Phi(r,t) + \mu_a\Phi(r,t) = S(r,t) \quad (3)$$

where r denotes the position vector of the photon, t is the instantaneous time at which the source is applied, c [m s^{-1}] is the speed of light in the medium, Φ is the photon fluence rate, defined as the energy flow per unit area per unit time in the given medium [W m^{-2}], S is the power of the light source [mW] operating at specific functional wavelength λ, and D is the photon diffusion coefficient, determined by Equation (4):

$$D = \frac{1}{3(\mu_a + \mu_s')} \quad (4)$$

where μ_a [m^{-1}] is the absorption coefficient and μs' [m^{-1}] is the reduced scattering coefficient of the medium at the wavelength λ of the light source. As evident from Equation (3), light propagation in a medium is governed by the absorption and scattering coefficients of the medium through which light propagates. In the model, a red LED emits light at 660 nm that diffuses first through air, crosses the PS multi-well bottom surface, and ultimately, reaches the cell in their culture medium. As the LED radiation traverses various layers, it undergoes Fresnel reflections at each boundary, modeled using the partial flux boundary condition, or Robin boundary condition. This condition establishes the relationship between fluence rate and its gradient at the boundary, crucial for accurately

**ADVANCED
SCIENCE NEWS**

www.advancedsciencenews.com

**ADVANCED
HEALTHCARE
MATERIALS**

www.advhealthmat.de

simulating light dynamics in the cell culture set-up, as outlined in Equation (5):[24,25,47,48]

$$\phi = z_b \, \hat{n} \nabla \phi \tag{5}$$

Here, $\hat{n}$ is the unit vector pointing from the inside of the first medium to the outside, and z_b is given by Equation (6):

$$z_b = \frac{2 l_{tr} \, (1 + R_{eff})}{3 \, (1 - R_{eff})} \tag{6}$$

where l_{tr} [m] is transport mean-free path, approximately $1/(\mu_a + \mu_s')$, and R_{eff} is the effective reflection coefficient to account for the refractive index mismatch between layers, defined as Equation (7):[24,25,47,48]

$$R_{eff} \approx \frac{-1.440}{n^2} + \frac{0.710}{n} + 0.668 + 0.00636 \, n \tag{7}$$

where n is the ratio of the index of refraction "inside" and "outside" the boundary: $n = n_{in}/n_{out}$. In the model, two crucial reflection coefficients were considered: one at the interface between air ($n_{in} = n_{air}$) and the PS 24-well plate ($n_{out} = n_{PS}$), and another between the PS ($n_{in} = n_{PS}$) and the cell feeding medium ($n_{out} = n_{DMEM}$). Solving the diffusion equation requires defining the absorption, scattering, and refraction coefficients of the optical media alongside characterizing light source intensity. The system employs seven adjacent LEDs emitting light at 660 nm, falling within the red visible spectrum. For air, at this wavelength, absorption, and scattering properties were considered negligible based on the literature.[22,23] The refractive index was set as $n_{air} = 1.00276$.[49,50] A PS cell culture multi-well has well-characterized light absorption properties.[51,52] Silva et al. characterized light absorption of the typical PS cell culture plate at 660 nm, reporting $\mu_a = 1.31 \ cm^{-1}$, with 78% effective transmission and 0.76 cm of penetration depth.[52] Scattering coefficient data of pure and bulky PS are more difficult to find, as most recent works focus on light scattering of PS nanoparticles in aqueous dispersions and not of the bulk material.[53,54] In an early work of Christ and Marhic,[55] the scattering and absorption properties of glassy PS were evaluated at $\lambda = 578$ nm, resulting in $\mu_a = 0.0004 \ cm^{-1}$ and $\mu_s' = 0.00024 \ cm^{-1}$. In a more recent study of Nguyen et al.,[56] 3D phantoms were built with acrylonitrile-butadiene-styrene plastic, with values of thickness similar to those of PS multi-well bottom surface. For these PS-based materials, absorption and scattering coefficient at $\lambda = 660$ nm were characterized, resulting in $\mu_a = 0.0005 \ cm^{-1}$ and $\mu_s' = 0.17 \ cm^{-1}$. Due to this great variability in absorption and scattering values, the PS layer was modeled with the absorption and scattering properties of the 3D phantom, being more similar to this case. The refractive index for PS was set as $n_{PS} = 1.583$.[57,58] The cell culture medium optical properties were approximated with those of salty water, with an absorption coefficient of $\mu_a = 0.0004 \ cm^{-1}$ and a scattering coefficient of $\mu_s' = 0.000008 \ cm^{-1}$.[59] The refractive index of DMEM was instead found to have a value of $n_{DMEM} = 1.3370$.[60]

Light propagation was modeled by making use of Helmholtz equation module in COMSOL Multiphysics 5.6 as it replicates the previously introduced DE. The general form of the Helmholtz equation in COMSOL is given by Equation (8):

$$\nabla \, (-c \nabla u) + au = f \tag{8}$$

where u represents the fluence rate, namely Φ in the DE, which is the dependent variable. Compared with the DE given by Equation (3), here diffusion coefficient D is given by "c", absorption coefficient μ_a is given by "a" and the source term S is "f". Since a stationary study (time-independent state) was carried out, the first term in Equation (3) gets eliminated.

Flux source boundary conditions, equivalent to the partial flux Robin boundary condition, were applied to each reflecting interface by setting boundary absorption/impedance terms as z_b, defined for the air-PS and for the PS-DMEM boundaries.[24] Table S3 (Supporting Information) resumes the parameters used for the numerical simulation. The source term was set according to the employed LEDs datasheet. For a forward current

of 450 mA, these LEDs generate a radiant flux of 682.5 mW; by increasing the current of 1 mA, the radiant flux increases by 0.3%. Thus, in the numerical simulation, source radiant flux conditions were varied to evaluate the optimal current to be used in the real set-up. Specifically, 682.5, 840, 997.5, 1155, and 1312 mW were set as source terms to solve the light diffusion equation.

ROS and Singlet Oxygen Production Upon Light Stimulation of Ang-Ce6-NLCs: Production of singlet oxygen from Ang-Ce6-NLCs after light irradiation was quantified using the probe DPBF, a singlet oxygen trapping agent strongly absorbing light at 415 nm and emitting bright bluish fluorescence. When DBPF reacts with singlet oxygen, it forms o-dibenzoylbenzene (DBB) by breaking the π-system of benzofuran and causing the inability of the product to absorb or emit visible light.[27] Hence, the reduction of absorbance of DPBF reflects the amount of singlet oxygen generated during PDT. Due to the solubility limitations of DPBF, all the experimental samples were dissolved in DMSO. In particular, the following experimental classes were considered: DPBF alone (50 µM), Ang-NLCs (357 µg mL^{-1}), Ce6 (2.5 µg mL^{-1}), Ang-Ce6-NLCs (357 µg mL^{-1}, corresponding to the loaded concentration of Ce6 of 2.5 µg mL^{-1}), Ang-NLCs (357 µg mL^{-1}) + DPBF (50 µM), Ce6 (2.5 µg mL^{-1}) + DPBF (50 µM), Ang-Ce6-NLCs (357 µg mL^{-1}). All samples were analyzed with a UV/visible spectrophotometer in the wavelength range of 300–800 nm, before and after irradiation. For the irradiation, all the samples were stimulated with the set-up previously described, at 660 nm, with a power intensity of 2 mW cm^{-2} for 60 s. Data were presented as absorption intensity reduction of DPBF at 415 nm in the samples after stimulation, in terms of percentage (%) with respect to the value before the stimulation, according to Equation (9):

$$\text{DPBF abs reduction} \quad (\%)$$
$$= \frac{\text{Intensity}_{\text{before irradiation}} - \text{Intensity}_{\text{after irradiation}}}{\text{Intensity}_{\text{before irradiation}}} \times 100 \tag{9}$$

Single oxygen generation in an aqueous environment was also investigated with the Singlet Oxygen Sensor Green Reagent (SOSG, Invitrogen). This probe displays a weak blue fluorescence; however, after reacting with singlet oxygen, it emits a green fluorescence ($\lambda_{ex} = 504$ nm, $\lambda_{em} = 525$ nm). All the samples were diluted in 1 mL of PBS at the following concentrations: Ang-NLCs (357 µg mL^{-1}), Ce6 (2.5 µg mL^{-1}), Ang-Ce6-NLCs (357 µg mL^{-1}, corresponding to the loaded concentration of Ce6 of 2.5 µg mL^{-1}). One microliters of a 5 mM stock solution of SOSG in methanol was added to all samples to obtain a final concentration of 5 µM. A control sample where only SOSG was diluted in PBS at the same concentration was also prepared. The fluorescence emission at 525 nm was measured with a spectrofluorometer (Agilent Technologies, Cary Eclipse); then, the samples were irradiated at 660 nm with a power intensity of 2 mW cm^{-2} for 60 s, and the fluorescence was measured again. Data were presented as increase of SOSG emission at 525 nm after stimulation, in terms of percentage with respect to the value before the stimulation, according to Equation (10):

$$\text{SOSG fluo increase} \quad (\%)$$
$$= \frac{\text{Emission}_{\text{after irradiation}} - \text{Emission}_{\text{before irradiation}}}{\text{Emission}_{\text{before irradiation}}} \times 100 \tag{10}$$

In order to understand the main mechanism of radical species production and the type of ROS produced upon light stimulation of Ang-Ce6-NLCs, the same experiments performed with the SOSG probe were also performed in the presence of specific ROS inhibitors, namely histidine and mannitol. Histidine is a well-known scavenger of both singlet oxygen and hydroxyl radicals,[28] while mannitol is specific for the hydroxyl radical.[29] The experiment was performed exactly in the same conditions as the test with SOSG; however, in this case, 5 mM of either L-histidine (Sigma–Aldrich) or mannitol (Sigma–Aldrich) were also added.

Release Studies: Release studies of Ce6 from the nanoparticles were performed by incubating 1 mg of Ang-Ce6-NLCs in different buffers (pH 4.5, pH 4.5 + 100 µM hydrogen peroxide, PBS, PBS + 100 µM hydrogen

peroxide) at 37 °C under gentle shaking and protected from light. At the selected timepoint (5, 24, 48, and 72 h), samples were collected, and centrifuged with Amicon Ultra4 filters (100 kDa) and at 4470 g for 40 min at 14 °C. The filtrate solution was collected and stored for Ce6 quantification, while the pellet was re-dispersed in its respective buffer and left under shaking until the consecutive timepoint. The amount of Ce6 released at each timepoint was quantified by HPLC, as previously explained, with calibration curves obtained for free Ce6 dispersed in each buffer. The cumulative release of Ce6 (%) over time was calculated by normalizing the amount of Ce6 released at each timepoint to the total amount of Ce6 loaded in the nanoparticles. The release experiments were also conducted upon light stimulation of the samples. At each timepoint, the solutions were irradiated in the set-up at 660 nm for 5 min, at a power density of 10 mW cm^{-2}.

Biocompatibility of Nanoparticles Without Light Irradiation: To understand the cytotoxic effects induced by the nanoparticles alone and choose a suitable concentration for the stimulation experiments, cell viability was tested upon administration of different nanoparticle concentrations, at both 24 h and 72 h, with the WST-1 assay (Roche), using U87 MG cells (ATCC HTB-14) as in vitro model for glioblastoma. U87 MG (15 × 10^3 cells cm^{-2}) were seeded in 24-well plates and cultured with high-glucose DMEM (Euroclone) added with 1% Penicillin-Streptomycin (Pen/Strep), 1% L-glutamine, 10% fetal bovine serum (FBS, Euroclone) to obtain complete medium. The following day, cells were treated with different concentrations of free Ce6 (0.7, 2.1, 3.5, and 7 µg mL^{-1}, diluted in complete DMEM from a stock solution of Ce6 5 mg mL^{-1} in DMSO), Ang-NLCs (100, 300, 500, and 1000 µg mL^{-1}), and Ang-Ce6-NLCs (100, 300, 500, and 1000 µg mL^{-1}, corresponding to the tested concentrations of "plain" Ce6) for 24 and 72 h. After the fixed incubation time, the media were removed, cells washed with PBS, and then incubated with 300 µL of phenol red-free complete DMEM with the WST-1 reagent (1:20 dilution) for 30 min at 37 °C. Thereafter, absorbance at 450 nm was measured using a PerkinElmer Victor X3 UV/visible spectrophotometer. The values were expressed as % with respect to untreated controls.

GBM Targeting Abilities of Ang-Ce6-NLCs: To investigate the targeting abilities of Ang-Ce6-NLCs, a dispersion of Vybrant-DIO-labeled Ang-Ce6-NLCs (100 µg mL^{-1}) were administered under flow conditions to various cell cultures mimicking the brain environments: human brain microvascular endothelial cells (hCMEC/D3, Millipore) cultured with EndoGrow complete medium kit (Millipore), human primary astrocytes (HA, Alphabioregen HBMP-202) cultured with Astrocytes Growth medium (Cell Alphabioregen), human neuron-like cells differentiated from SHSY5Y (ATCC CRL-2266) cultured with DMEM F12 (Gibco), primary human brain microglia (HBPM, Alphabioregen PHM001) cultured with Alpha-Glia Expansion Medium (Alphabioregen), pericytes (HBVP ScienCell, 1200-SC) cultured with Pericyte Medium (Alphabioregen), and GBM cell model (U87 MG, ATCC, HTB-14) cultured with complete DMEM. 15 × 10^3 hCMEM/D3, astrocytes, microglia, pericytes, or U87 MG cells were seeded on 1 cm^2 round glass coverslips (VWR) 24 h prior to the experiment. Human neuron-like cells were derived from SH-SY5Y; 10^4 SH-SY5Y were seeded 8 days before the experiment on 1 cm^2 round glass coverslips, in DMEM F12 (Gibco) with 1% glutamine (Sigma–Aldrich), 10% FBS (Sigma–Aldrich), and 1% Pen/Strep (Gibco). After 48 h, the differentiation of the cells was induced by replacing the culture medium with high-glucose DMEM (Euroclone) with 1% FBS, 1% glutamine, 1% Pen/Strep, and 10^{-5} M retinoic acid (Thermo Scientific); these culture conditions were maintained for 6 days.

On the day of the experiment, glass coverslips with the different cultures were placed in a custom fluidic bioreactor designed for targeting experiments, as reported in the previous work.[12] Vybrant DiO-labeled Ang-Ce6-NLCs or Ce6-NLCs (100 µg mL^{-1}) in complete phenol red-free DMEM and supplemented with HEPES were perfused through the bioreactor at a rate of 12 mL min^{-1} for 3 h at 37 °C. After the experiment, cells were washed with PBS and fixed with 4% paraformaldehyde (PFA) at 4 °C for 30 min, followed by staining with TRITC-phalloidin 0.5% (Sigma–Aldrich) and Hoechst 33342 0.1% (Invitrogen) in PBS for 30 min at 37 °C, to label cytoskeletal actin and nuclei, respectively. Confocal microscopy was performed with a C2s confocal microscope (Nikon), and the analysis

of internalization was based on the colocalization of nanoparticle signal (green) with that one of the cytoskeletal actin (red).

Ang-Ce6-NLCs Cell Uptake and Intracellular Fate: Ang-Ce6-NLCs uptake pathway was investigated by confocal microscopy, considering pinocytosis and clathrin- and caveolin-mediated endocytosis. U87 MG cells were seeded in WillCo-Dish (glass bottom dish, WillCo wells BV) at a density of 10^4 cells cm^{-2}.

For pinocytosis, the day after seeding, the cells were incubated with 100 µg mL^{-1} of Vybrant DIO-labeled Ang-Ce6-NLCs, together with the Cascade Blue hydrazide fluorescent dye (1:40, Invitrogen), for 6 and 24 h at 37 °C. In the end, cells were washed three times with PBS and finally left in a fresh phenol red-free HEPES-supplemented complete medium. Confocal images were acquired immediately, and a co-localization analysis (Pearson's correlation coefficient) between signals of Ang-Ce6-NLCs and of pinosomes was performed by NIS-Elements software.

To study caveolin and clathrin-mediated endocytosis, after seeding in WillCo dishes, U87 MG cells were treated with 100 µg mL^{-1} of Vybrant DIO-labeled Ang-Ce6-NLCs for 6 and 24 h at 37 °C. After incubation, cells were washed with PBS and fixed with 4% PFA at 4 °C for 30 min. Subsequently, cells underwent three washes with PBS and then incubated with a blocking solution based on goat serum (GS, 10%, EuroClone) and Triton X-100 (diluted 1:1000, Sigma–Aldrich) in PBS for 30 min. Subsequently, samples were treated with either anti-caveolin-1 primary antibody (1:150, Abcam) or anti-clathrin primary antibody (1:150, Abcam) in PBS containing 10% GS for 2 h. Following three washes with 10% GS in PBS, the samples were stained for 1 h with Alexa-Fluor-488 secondary antibody (1:250, Millipore), TRITC-phalloidin (1:200, Sigma–Aldrich), and Hoechst 33342 (1:1000, Invitrogen). Samples were then rinsed three times with PBS and finally analyzed using confocal microscopy. Co-localization analysis, assessed by Pearson's correlation coefficient, was performed using NIS-Elements software.

To understand the intracellular fate of Ang-Ce6-NLCs, their uptake in lysosomes and late endosomes was studied by confocal fluorescence microscopy. U87 MG cells were seeded in WillCo Petri dishes at a density of 10^4 cells cm^{-2} and incubated, after 24 h, with 100 µg mL^{-1} of Vybrant DIO-labeled Ang-Ce6-NLCs for 24 and 48 h at 37 °C. After the incubation, the samples were washed twice with PBS and treated with the LysoTracker Deep Red dye (1:2000, Invitrogen) in a high-glucose phenol red-free HEPES-supplemented complete medium for 30 min. Then, the cells were washed and stained with Hoechst 33342 (1:1000, Invitrogen) for 15 min at 37 °C. Confocal fluorescence microscopy and co-localization analysis were performed as previously described.

Effect of Ang-Ce6-NLCs-Mediated PDT on GBM Cell Viability: For the evaluation of GBM cell viability after light exposure at different power densities, U87 MG cells were seeded in 24-well at 15 × 10^3 cells cm^{-2}. The following day, cells were treated with either 0.7 µg mL^{-1} of free Ce6 or 100 µg mL^{-1} Ang-Ce6-NLCs for 24 h. After incubation, the media were replaced with fresh culture medium without any photosensitizer. Cells were then irradiated in the set-up at 660 nm for 5 min, testing three different power densities: 20, 10, or 2 mW cm^{-2} (corresponding to light doses of 6, 3, and 0.6 J cm^{-2}). After stimulation, WST-1 assay was performed as described above.

To study the effect of PDT on U87 MG cell proliferation and apoptosis, the expression of p53 (apoptosis) and Ki-67 (proliferation) markers was investigated by immunofluorescence after the treatment with free Ce6 or Ang-Ce6-NLCs, with or without light irradiation. U87 MG cells were seeded at 15 × 10^3 cells cm^{-2} in a 24-well plate where glass slides were previously inserted. Then, cells were treated with either 0.7 µg mL^{-1} of free Ce6, 100 µg mL^{-1} Ang-NLCs, or 100 µg mL^{-1} Ang-Ce6-NLCs for 24 h. At the end of the incubation, the media were replaced with fresh medium without any photosensitizer. Cells were then irradiated in the set-up at 660 nm for 5 min at 10 mW cm^{-2} (selected based on the results of the WST-1 assay). The same experimental classes without light stimulation were also investigated, together with control U87 MG cells (with or without light irradiation). After 1 h, cells were fixed with 4% PFA at 4 °C for 20 min. Then, cells were incubated for 30 min with a blocking solution (GS 10% and 1:1000 Triton-X 100) and then incubated with a primary anti-Ki-67 rabbit antibody (1:200, Millipore) and a primary

**ADVANCED
SCIENCE NEWS**

www.advancedsciencenews.com

**ADVANCED
HEALTHCARE
MATERIALS**

www.advhealthmat.de

anti-p53 mouse antibody (1:200, Abcam) for 2 h at 37 °C. Afterward, cells were washed and incubated for 1 h with a FITC-conjugated secondary anti-rabbit antibody (1:250 dilution, for Ki-67 staining, Millipore), and with a TRITC-conjugated secondary anti-mouse antibody (1:250, for p53 staining, Millipore). In the end, cell nuclei were counter-stained with Hoechst 33342 (1:1000, Invitrogen) for 20 min. Imaging was performed with the confocal microscope and the analysis of the p53 and Ki-67 positive nuclei was carried out with NIS-Elements software (Nikon).

Induction of Intracellular Oxidative Stress by Ang-Ce6-NLCs-Mediated PDT: The induction of oxidative stress at the mitochondrial level was investigated through the assessment of increased expression of mitochondrial heat shock protein 90 (HSP90), also known as TRAP1. 15×10^3 cells cm^{-2} U87 MG cells were seeded on glass slides, previously inserted in a 24-well plate and then treated with either 0.7 µg mL^{-1} of free Ce6, 100 µg mL^{-1} Ang-NLCs, or 100 µg mL^{-1} of Ang-Ce6-NLCs for 24 h. The following day, the media were replaced with fresh medium, and cells were irradiated with 660 nm-light for 5 min at 10 mW cm^{-2}. The same experimental classes without light stimulation were also investigated, together with control U87 MG cells (with or without light irradiation). After 1 h, samples were fixed with 4% PFA at 4 °C for 20 min. Subsequently, cells were washed with PBS, treated with 10% GS, and stained with Hoechst 33342 (1:1000) for 30 min at 37 °C. A primary rabbit antibody against TRAP1 (GeneTex) at a dilution of 1:300 in 10% GS was then incubated for 2 h at 37 °C. Following three washes, a FITC-conjugated goat anti-rabbit secondary antibody (Invitrogen) at a dilution of 1:250 in 10% GS was incubated for 2 h at 37 °C. Images were obtained by confocal microscopy, following the previously described procedure. For each image, the total fluorescence intensity corresponding to the TRAP1 channel was quantified with ImageJ, normalized by the number of cells in the measured area, and presented as "TRAP1-intensity"). To better highlight the effect of the treatment, for each experimental class, TRAP1-intensity was normalized to the value found for the untreated control and expressed as -fold change with respect to the control.

Migration Properties of U87 MG Cells from U87 MG-Derived Spheroids after Ang-Ce6-NLCs-Mediated PDT: U87 MG spheroids were obtained by culturing U87 MG cells (10.8×10^4 cells per well) in 48-well plates, previously coated with 200 µL of 2% agarose gel in ultrapure water. After 5 days, 3D spheroids were obtained, and six spheroids for each experimental class were collected and allowed to adhere to the bottom of the 24-well. Eight experimental classes were considered: untreated spheroids -control-, control + light, 0.7 µg mL^{-1} of free Ce6, 0.7 µg mL^{-1} of free Ce6 + light, 100 µg mL^{-1} of Ang-NLCs, 100 µg mL^{-1} of Ang-NLCs + light, 100 µg mL^{-1} of Ang-Ce6-NLCs (corresponding to 0.7 µg mL^{-1} of Ce6), 100 µg mL^{-1} of Ang-Ce6-NLCs + light). After 24 h of treatment, the media were replaced with 500 µL of free phenol red fresh medium to all experimental classes, and light stimulation at 660 nm for 5 min at 10 mW cm^{-2} was performed. Images of the spheroids were taken by bright-field microscopy before and at 24, 48, and 72 h after the stimulation, and subsequently analyzed with the ImageJ software in terms of "migration area", defined as the area occupied by the cells migrating from the core of the spheroid, and calculated by subtracting the area of the core of the spheroid to the total area occupied by the migrating cells plus the spheroid (Figure S23, Supporting Information).[61–63]

Proteomic Analysis: To thoroughly characterize the molecular impact of PDT, and of every component of it separately, a proteomics investigation based on mass spectrometry (MS) was conducted. Proteomics-dedicated U87 MG spheroids, obtained as described above, were derived from a single cell aliquot, cultured in various conditions and timing to produce all necessary experimental classes, each of which consisting of 10 spheroids. From that initial aliquot, cells were cultured in 5 sequential batches, each composed of 8 samples varying in treatment regimes. More precisely, batches 4 and 5 both represent experimental endpoint, being technical replicas of each other that was included as a control.

Through three alternative analytical strategies, which are referred to as sub-studies, proteomics variations associated with therapy, culture passage, or both were dissected. Specifically, sub-studies α (the main one) and β evaluate the impact of treatment, respectively in the presence or the absence of passage variations. Sub-study γ is instead dedicated to the

characterization of the effects of time per se. **Table 3** details on proteomics classes and replicas. For all the experimental classes, fresh medium was replaced 24 h post-treatment, and samples receiving light stimulation were irradiated at 660 nm for 5 min at 10 mW cm^{-2}. After 1 h, spheroids were washed with PBS, collected in sterile tubes by removing excess PBS, and stored at −80 °C until further analysis.

Proteomics Data Acquisition: Samples were lysed, reduced, and alkylated in 100 µL LYSE buffer (Preomics) at 95 °C for 10 min. Then, they were sonicated with an Ultrasonic Processor UP200St (Hielscher), 3 cycles of 30 s. The protein amount of lysates was measured by the Tryptophan method.[64] Proteins were isolated and digested by the protein aggregation capture method automated on a KingFisher Apex robot (Thermo Fisher Scientific) in 96-well format as described in Bekker-Jensen et al.[65] Briefly, the tip plate was stored in plate #1. Lysate samples were stored in plate #2, at a final concentration of 70% acetonitrile, and with magnetic beads in a protein/bead ratio of 1:4 (1:1 SpeedBead magnetic carboxylate 45152105050250 and 65152105050250, Cytiva). Washing solutions were in plates #3–5 (acetonitrile), plate #6 (70% ethanol), and plate #7 (isopropanol). Plate #8 contained 100 µL of digestion solution, namely 25 mm Tris HCl pH 8, endoproteinase LysC (Wako) in an enzyme/protein ratio of 1:100 (w/w), and trypsin (Promega) in an enzyme/protein ratio of 1:50. Protein aggregation was carried out in two steps, each composed of a 1 min mixing at medium speed followed by a 10 min pause. Sequential washes were performed in 2.5 min at a slow speed, without releasing the beads from the magnet. Digestion was set to 2.5 h, at 37 °C and at slow speed.

Resulting peptides were analyzed on the Evosep One system using an EASY spray column (150 µm × 15 cm, 2 µm particle size, Thermo Scientific) and the pre-programmed gradient of 30 samples per day, with a flow rate of 0.5 µL min^{-1}. The column temperature was maintained at 40 °C and interfaced online with the Orbitrap Exploris 480 MS (Thermo Scientific) with FAIMS Pro Duo Interface (Thermo Scientific). MS analysis was performed in data-independent acquisition (DIA) mode. High-field asymmetric waveform ion mobility spectrometry compensation voltage was set to −45 at standard resolution. Full MS resolution was set to 120 000 in a range between 375 and 1500 m/z, with a Normalized AGC target set to 300%, and a maximum injection time set to Auto. The normalized AGC target for fragment spectra was set at 1000%, using 40 windows of 15 m/z with an overlap of 1 m/z. Resolution was set to 30 000, and injection time to Auto. The normalized collision energy was set at 30%. All data were acquired in profile mode using positive polarity.

All DIA raw files were processed with Spectronaut version 18 using a library-free approach (directDIA) with default settings.[66] Enzymes / Cleavage Rules was set to Trypsin/P, LysC. The library was generated against the Uniprot Human database (release UP000005640_9606 November 2022, 102572 entries). Carbamidomethylation was selected as a fixed modification, and methionine oxidation and N-terminal acetylation as variable modifications. The significance cutoff for false discovery rates (FDRs) of peptide-spectrum matches and peptide/protein groups was set to 0.01. Precursor Filtering for quantification was set to Identified (Qvalue), and the Imputation Strategy was set to Run Wise Imputing. MS2 was chosen as quantity MS-level.

Principal Component Analysis: Statistical analyses on the Spectronaut Protein Quant Pivot Report were performed via Perseus 1.6.15.0.[67] A PCA score plot, yielding information about sample diversity depending on treatment type and time point, is part of Perseus' output.

Pairwise Comparisons Across Proteomics Classes: Pairwise comparisons were conducted across selected experimental classes, using normalized class-mean relative protein abundances (RPAs). For sub-studies α and γ, Student's t-tests were systematically utilized to evaluate each RPA variation on the comparison at hand, setting the threshold for significance on p-values to 0.05. FDRs (permutation-based, 0.05 cutoff for significance on q-values) were applied on successful t-tests, to mitigate multiple comparisons problem. Artificial variance within-groups (s0) was set to 0.1. For sub-study β, due to its limited number of replicas, the effects of treatment were evaluated through significance B tests, with a significance threshold for Benjamini-Hochberg FDRs set to 0.05. Comparisons considered for

**ADVANCED
SCIENCE NEWS**

www.advancedsciencenews.com

**ADVANCED
HEALTHCARE
MATERIALS**

www.advhealthmat.de

each of the three sub-studies are reported in Table S2 (Supporting Information). Proteins displaying significantly different abundances, which are called differentially represented proteins (DRPs), are either over- or under-represented in the first term of the comparison. For each of the considered comparisons, in addition to full DRP sets trend-specific lists were prepared featuring only up- or down-regulated proteins.

Protein Overlap Among Pairwise Comparisons: Sets of DRPs resulting from pairwise comparisons among proteomics experimental classes were intersected and visualized as Venn diagrams, also evaluating the consistency of each DRP at a given intersection in terms of up- or down-regulation trends. A shared DRP was deemed consistent if systematically up- or systematically down-regulated in all parent sets involved, at least when these are overlaid on the basis of the experimental variables they investigate.

Hierarchical Clustering, and Gene Ontology: Other analyses were carried out as convenient to further characterize specific groups of proteins. Proteins/DRPs within a list of interest were hierarchically clustered based on their RPAs across different samples or classes, which were hierarchically clustered as well based on their overall proteome/protein-set similarities. The two dendrograms yielded by such HC procedure were utilized to define rows and columns of a central heatmap, color-coding individual RPAs. GO investigations were undertaken to unveil processes (GO biological process), functions (GO molecular function), or components (GO cellular components) relevantly associated with a given set of proteins/DRPs. These were performed with GOrilla,[68] set to target-and-background-lists modality, using as a background the whole list of human genes, fetched from Ensembl BioMart.[69,70] All GO terms found to be significantly enriched – imposing significance thresholds of 0.05 to both *p*- and *q*-values – were submitted to REVIGO, to be rendered as scatter plots. Final polishing was done on Cytoscape 3.10.2.[71]

Ang-Ce6-NLCs-Mediated PDT in the Neurovascular Unit Sensorized In Vitro Model: To evaluate the effect of PDT in a complex system that recapitulates the in vitro GBM microenvironment, together with typical healthy brain cells populating the brain parenchyma and the blood-brain barrier structure (BBB), a biomimetic neurovascular unit model was developed. This bioreactor was designed for multi-cultures of human astrocytes, human microglia, and human neuron-like cells, alongside U87 MG cells. The bioreactor is assembled through three poly(methyl methacrylate) (PMMA) sheets of different thickness combined in order to obtain a 5 mm thick composite piece with an internal channel 0.5 mm high and on the bottom separated by a 2 mm poly(dimethyl siloxane) (PDMS, 1:10, SYLGARDTM 184) gaskets, combined with a 7 mm thick composite piece with a 2 mm deep chamber specially cut according to the specific design. The different sheets were joined together by external aluminum frames and closed with screws. The bioreactor is composed of two areas dedicated to cell cultures, an upper fluidic channel (5 mm wide, 105 mm long, and 0.75 mm high) organized as a "zig-zag" serpentine with 3 arms and connected with two outlets to a pump system. A static lower rectangular chamber (25 mm wide, 110 mm long, and 2 mm high) simulates healthy or GBM-affected brain tissue. A 3 μm cut-off porous poly(ethylene terephthalate) (PET) membrane sheet was placed between the channel and the chamber interface to separate the area of the BBB from the healthy brain tissue (Figure S18, Supporting Information).

The entire bioreactor (80 mm × 150 mm side × 15 mm height) has been designed to be inserted inside the LED stimulation device, and has been equipped with two types of sensors: an electronic sensor composed of a couple of electrodes, one on the top channel and the other placed 5 mm below, on the other side of the BBB model, for a measurement of the TEER, adapting electrodes for the epithelial Volt-Ohm Meter (Millicell ERS-2, Millipore), and a thermal sensor, consisting of a thermocouple integrated in the lower chamber to follow real-time the temperature inside the bioreactor. The bioreactors were connected in series with a homemade pumping system to automatically change cell culture media, with a 12 mL min⁻¹ flow rate.

Simulation of the Fluid Dynamics: COMSOL Multiphysics software was used to simulate the fluid dynamics in the bioreactor top compartment to validate its design. Selecting the "Laminar Flow (spf)" interface, velocity, and pressure fields were computed for single-phase fluid flow in the laminar regime, determining fluid dynamic shear-stress at the bottom wall where cells are seeded. Laminar flow persists if the Reynolds number (*Re*) remains below 2300.[72] At higher Reynolds numbers (*Re* > 2900), disturbances grow and cause a transition to turbulence. The critical Reynolds number varies based on model parameters, as indicated by Equation (11):

$$Re = \frac{\rho \langle v \rangle D_H}{\mu} \tag{11}$$

where ρ [kg m⁻³] is the fluid density, $\langle v \rangle$ [m s⁻¹] is the average fluid velocity along the duct, μ is the dynamic viscosity of the fluid [Pa·s], and D_H [m] is the hydraulic diameter of the duct that, for a rectangular geometry, is defined as $D_H = 4 \frac{A}{P}$,[73] with A being the cross-sectional area of the duct and P its perimeter. The average fluid velocity $\langle v \rangle$ along the principal direction depends on the flow rate at the inlet of the chamber Q_i [m³ s⁻¹], as well as on the sizes of the flow chamber, i.e., the height h and the width w, as defined by $\langle v \rangle \geq \frac{Q_i}{h\,w}$.

For incompressible Newtonian fluids flowing upon a planar surface, fluid dynamic shear-stress is determined according to Newton's law by Equation 12:[74]

$$\tau_{ij} = - \mu \frac{dv_i}{dj} \tag{12}$$

where μ is the fluid dynamic viscosity and $\frac{dv_i}{dj}$ is the gradient of the ith fluid velocity along the jth directions. Under the laminar and stationary flow hypothesis, between two parallel plates (distant h from each other and with a specific width w and length l, with $l >> w >> h$), the wall shear stress (WSS) can be analytically derived, assuming Equation (13):[75]

$$WSS = \langle v \rangle \frac{6\mu}{h} \tag{13}$$

where $\langle v \rangle$ is the average fluid velocity along the flowing direction; this depends on the flow rate at the chamber inlet (Q_i) and on the flow chamber sizes h and w. Using COMSOL Multiphysics, shear stress value is derived from the velocity field.

Assuming laminar flow along the *x*-axis with no-slip conditions at the walls, the COMSOL Laminar Flow interface computes velocity, pressure fields, and shear stress (including that one at the duct wall). The simulation was run by varying the inlet flow rate (Q_i), from 1.2 to 12 mL min⁻¹ (inlet flow rate in the cylindrical graft), to evaluate the optimal flow rate to achieve the desired shear stress on cells. Outlet condition was maintained as *P|out* = 0 Pa (outlet pressure); the flowing material (cell culture medium, density 993 kg m⁻³ and viscosity 8.9•× 10⁻⁴ Pa s) was considered an incompressible and Newtonian fluid. The channel height was fixed as *h* = 0.5 mm and the width at 5 mm. Mesh of tetrahedral finite elements defined the fluid dynamic domain, computing spatial velocity distributions within the micrometric culture channel.

Population of the Bioreactor with Different Cell Lines: Cells in the bioreactor were seeded starting from the upper channel. hCMEC/D3 (40 × 10³ cells cm⁻²) were seeded in EndoGrow complete culture medium; 5 × 10³ cells cm⁻² of human primary astrocytes and 5 × 10³ cells cm⁻² of human primary pericytes were seeded together in Astrocytes Growth medium (Cell Application, Inc.) in the bottom part of the porous membrane. The co-culture was grown for 5 days, when the endothelial cells formed a compact monolayer on the membrane, mimicking the BBB. Contextually, 10 × 10³ cells cm⁻² of SH-SY5Y in high-glucose DMEM 1% FBS were seeded on rectangular glass coverslips (54 × 24 mm, Menzel-Gläser), and then retinoic acid 1:1000 was added for 6 days to foster differentiation in neuron-like cells. One day before the integration in the bioreactor, another rectangular glass coverslips (54 × 24 mm, Menzel-Gläser) was seeded with 15 × 10³ cells cm⁻² of U87 MG cells. Human primary microglia (5 × 10³ cells cm⁻²) and human primary astrocytes (5 × 10³ cells cm⁻²) were, instead, seeded on the same glasses previously populated with neuron-like cells, in high-glucose complete DMEM. On the day of

2402823 (23 of 25)

the integration, the bioreactor was opened and one glass with healthy co-cultures and one glass with GBM cells were added to the bottom camber. After 6 h from the integration, the bioreactors were connected with a pump system.

Only for imaging purposes, to better characterize the morphology of the formed BBB, GFP-expressing primary human astrocytes (Alphabioregen HBMP201-F) were employed. The cells were fixed with 4% PFA for 20 min and the samples were stained with TRITC-phalloidin and Hoechst 33342, as previously reported, and images were acquired by confocal microscope.

ZO-1 expression was also assessed by immunofluorescent staining; the fixed BBB models were removed from the bioreactor and collected in 3 cm diameter petri dish, and treated with PBS + Triton X100 (1:1000, Sigma–Aldrich) solution for 10 min, and later with GS/PBS (1:10, Sigma–Aldrich) solution for 30 min at 37 °C. Then, samples were incubated for 2 h at 37 °C with 2 mL of rabbit anti-ZO-1 primary antibody (1:300, Invirogen) in GS 10%. After 3 washing steps with GS 10%, 2 mL of FITC-conjugated goat anti-rabbit secondary antibody in GS 10% was added, and incubated for 2 h at 37 °C. In the end, nuclei were counter-stained with Hoechst 33342 (1:1000), while the cytoskeleton was stained with TRITC-phalloidin, as previously described. Images were acquired with the confocal microscope.

PDT Experiments with the Bioreactor: For PDT experiments, four experimental conditions were considered, using four different bioreactors: control, control + light, Ang-Ce6-NLCs, Ang-Ce6-NLCs + light. The culture medium of the channels was maintained and connected to the fluidic pump system, while the culture medium in the bottom chamber (GBM and healthy brain cells compartment) was replaced with a dispersion of 100 µg mL^{-1} of Ang-Ce6-NLCs in complete medium for 24 h (or just complete DMEM in the case of controls). On the day of the experiment, the TEER was measured, the culture medium of the bottom chamber was removed, the co-cultures were washed with PBS, and fresh complete DMEM without phenol red was added. The bioreactors were disconnected from the fluidic pump system, placed in the irradiation set-up, and stimulated at 660 nm, 10 mW cm^{-2} at 37 °C for 5 min. Dark controls were left inside the incubator. During the light exposure, the temperature profile was followed. After 1 h from the stimulation, the bioreactor was disassembled to analyze each component individually. In particular, the metabolic activity of the cells (BBB, healthy brain cells, and GBM cells) was evaluated with the WST-1 assay as previously described. To evaluate the cytotoxic effects of the PDT treatment, the co-cultures that exhibit a reduction of viability (GBM cell culture and healthy brain cells) were also analyzed with the Live/Dead assay Kit (Thermofisher). Cells were incubated with calcein AM $4 \cdot \times 10^{-9}$ M (ThermoFisher Scientific), ethidium homodimer-1 $4 \cdot \times 10^{-9}$ M (Thermoscientific), and Hoechst 33342 $20 \cdot \times 10^{-6}$ M (Invitrogen) for 40 min. Confocal acquisitions were performed after PBS washing and images were analyzed with ImageJ to count the ratio of the number of dead cells with respect to the number of total nuclei. The data were indicated as % of dead cells with respect to the total number of cells in each sample.

Statistical Analysis: All the data presented in this work are presented as means of at least three separate repetitions (n), and the error bars represent their standard deviations (SD). Statistical analyses for proteomics are reported within the pertinent paragraphs. All other statistical evaluations of normally distributed data were done by one-way ANOVA followed by Bonferroni's means comparison by using OriginLab Software. Only for the migration assay, data were analyzed by Kruskal-Wallis ANOVA with OriginLab Software. In all cases, significance was defined as $p \leq 0.05$.

Supporting Information

Supporting Information is available from the Wiley Online Library or from the author.

Acknowledgements

Conflict of Interest

The authors declare no conflict of interest.

Data Availability Statement

All mass spectrometry proteomics data have been deposited to the ProteomeXchange Consortium via the PRoteomics IDEntifications (PRIDE) database[76] (Identifier: PXD053482). All other data are presented in the manuscript or its Supporting Information.

Keywords

[1] H. Xu, J. Chen, H. Xu, Z. Qin, *Front Aging Neurosci* **2017**, *9*, 1.

[2] A. Degl'Innocenti, N. di Leo, G. Ciofani, *Adv Ther (Weinh)* **2020**, *3*, 1900152.

[3] A. D'Alessio, G. Proietti, G. Sica, B. M. Scicchitano, *Pathological and Molecular Features of Glioblastoma and its Peritumoral Tissue*, Vol. 11, Multidisciplinary Digital Publishing Institute, **2019**, p. 469.

[4] W. M. Pardridge, *Pharm. Res.* **2007**, *24*, 1733.

[5] R. R. Allison, K. Moghissi, *Clin Endosc* **2013**, *46*, 24.

[6] C. Pucci, C. Martinelli, A. Degl'Innocenti, A. Desii, D. De Pasquale, G. Ciofani, *Macromol. Biosci.* **2021**, *21*, 2100181.

[7] A. Hak, M. S. Ali, S. A. Sankaranarayanan, V. R. Shinde, A. K. Rengan, *ACS Appl Bio Mater* **2023**, *6*, 349.

[8] Y. Li, P. Wang, X. Wang, X. Su, Q. Liu, *Ultrasound Med Biol* **2014**, *40*, 990.

[9] J. M. Fernandez, M. D. Bilgin, L. I. Grossweiner, *J Photochem Photobiol B* **1997**, *37*, 131.

[10] L. Maletínská, E. A. Blakely, K. A. Bjornstad, D. F. Deen, L. J. Knoff, T. M. Forte, *Cancer Res.* **2000**, *60*, 2300.

[11] M. M. Kim, A. Darafsheh, *Photochem. Photobiol.* **2020**, *96*, 280.

[12] C. Pucci, D. De Pasquale, A. Marino, C. Martinelli, S. Lauciello, G. Ciofani, *ACS Appl. Mater. Interfaces* **2020**, *12*, 29037.

[13] Y. Kato, S. Ozawa, C. Miyamoto, Y. Maehata, A. Suzuki, T. Maeda, Y. Baba, *Cancer Cell Int.* **2013**, *13*, 89.

[14] S. Trapp, G. R. Rosania, R. W. Horobin, J. Kornhuber, *Eur. Biophys. J.* **2008**, *37*, 1317.

[15] N. Yang, W. Xiao, X. Song, W. Wang, X. Dong, *Nanomicro Lett* **2020**, *12*, 1.

[16] J. Q. Cai, X. M. Liu, Z. J. Gao, L. L. Li, H. Wang, *Mater. Today* **2021**, *45*, 77.

[17] M. Gouterman, *J. Mol. Spectrosc.* **1961**, *6*, 138.

[18] M. Gouterman, *J. Chem. Phys.* **1959**, *30*, 1139.

[19] Y. Liu, K. Ma, T. Jiao, R. Xing, G. Shen, X. Yan, *Sci. Rep.* **2017**, *7*, 1.

[20] A. A. Frolov, E. I. Zenkevich, G. P. Gurinovich, G. A. Kochubeyev, *J Photochem Photobiol B* **1990**, *7*, 43.

[21] B. Čunderlíková, L. Gangeskar, J. Moan, *J Photochem Photobiol B* **1999**, *53*, 81.

[22] W. Zhang, B. Hu, C. Chen, P. Du, L. Zhang, G. Feng, *Adv Atmos Sci* **2004**, *21*, 848.

[23] S. Mogo, V. E. Cachorro, M. Sorribas, A. de Frutos, R. Fernández, *Geophys. Res. Lett.* **2005**, *32*, L13811.

[24] V. Vysakh, N. U. Sujatha, *Light-Tissue Interaction Modeling Using COMSOL Multiphysics for Multi-layered Soft Tissues*, **2018**.

[25] S. A. M. Kirmani, L. Velmanickam, D. Nawaratha, S. S. Sherif, I. T. Lima Jr., *Simulation of Diffuse Optical Tomography using COMSOL Multiphysics*, **2016**.

[26] A. Bansal, F. Yang, T. Xi, Y. Zhang, J. S. Ho, *Proc. Natl. Acad. Sci. USA* **2018**, *115*, 1469.

[27] X.-F. Zhang, X. Li, *J. Lumin.* **2011**, *131*, 2263.

[28] A. M. Wade, H. N. Tucker, *J. Nutr. Biochem.* **1998**, *9*, 308.

[29] B. Shen, R. C. Jensen, H. J. Bohnert, *Plant Physiol.* **1997**, *115*, 527.

[30] H. Liu, P. J. H. Carter, A. C. Laan, R. Eelkema, A. G. Denkova, *Sci. Rep.* **2019**, *9*, 8393.

[31] S. Paul, P. W. S. Heng, L. W. Chan, *J Fluoresc* **2013**, *23*, 283.

[32] K. Sakamoto, T. Shinohara, Y. Adachi, T. Asami, T. Ohtaki, *Biochem Biophys Rep* **2017**, *12*, 135.

[33] J. Guyon, C. Chapouly, L. Andrique, A. Bikfalvi, T. Daubon, *Front Physiol* **2021**, *12*, 622615.

[34] I. Masgras, C. Sanchez-Martin, G. Colombo, A. Rasola, *Front Oncol* **2017**, *7*, 58.

[35] G. Hua, Q. Zhang, Z. Fan, *J. Biol. Chem.* **2007**, *282*, 20553.

[36] F. Torrisi, C. Alberghina, S. D'aprile, A. M. Pavone, L. Longhitano, S. Giallongo, D. Tibullo, M. Di Rosa, A. Zappalà, F. P. Cammarata, G. Russo, M. Ippolito, G. Cuttone, G. Li Volti, N. Vicario, R. Parenti, *Biomedicines* **2022**, *10*, 806.

[37] A. Hatoum, R. Mohammed, O. Zakieh, *Cancer Manag Res* **2019**, *11*, 1843.

[38] E. I. Fomchenko, E. C. Holland, *Clin. Cancer Res.* **2006**, *12*, 5288.

[39] I. Papademetriou, E. Vedula, J. Charest, T. Porter, *PLoS One* **2018**, *13*, e0205158.

[40] DOE Fundamentals Handbook, Thermodynamics, Heat Transfer, and Fluid Flow, Volume 1 of 3, US Department of Energy **1996**.

[41] A. D. Wong, M. Ye, A. F. Levy, J. D. Rothstein, D. E. Bergles, P. C. Searson, *Front. Neuroeng.* **2013**, *6*, 7.

[42] A. Mehta, A. Desai, D. Rudd, G. Siddiqui, C. J. Nowell, Z. Tong, D. J. Creek, P. Tayalia, P. S. Gandhi, N. H. Voelcker, *Adv Biol* **2022**, *6*, 2200152.

[43] H. C. Helms, N. J. Abbott, M. Burek, R. Cecchelli, P. O. Couraud, M. A. Deli, C. Förster, H. J. Galla, I. A. Romero, E. V. Shusta, M. J. Stebbins, E. Vandenhaute, B. Weksler, B. Brodin, *J. Cereb. Blood Flow Metab.* **2015**, *36*, 862.

[44] J. Barsotti, A. G. Rapidis, I. Hirata, F. Greco, F. Cacialli, V. Mattoli, *Adv. Electron. Mater.* **2021**, *7*, 2001145.

[45] L. V. Wang, H. Wu, in *Biomedical Optics: Principles and Imaging*, John Wiley & Sons, Inc. Hoboken, New Jersey **2007**, pp 343.

[46] T. Lister, P. A. Wright, P. H. Chappell, *J. Biomed. Opt.* **2012**, *17*, 090901.

[47] T. Durduran, R. Choe, W. B. Baker, A. G. Yodh, *Rep Prog Phys* **2010**, *73*, 076701.

[48] M. Dhmiri, Y. Manai, T. Ezzedine, *2023 International Symposium on Networks, Computers, and Communications*, **2023**.

[49] P. E. Ciddor, *Appl. Opt.* **1996**, *35*, 1566.

[50] A. Börzsönyi, Z. Heiner, M. P. Kalashnikov, A. P. Kovács, K. Osvay, *Appl. Opt.* **2008**, *47*, 4856.

[51] A. N. Sabbar, H. S. Mohammed, A. R. Ibrahim, H. R. Saud, *Orient. J. Chem.* **2019**, *35*, 455.

[52] D. F. T. Silva, R. A. Mesquita-Ferrari, K. P. S. Fernandes, M. P. Raele, N. U. Wetter, A. M. Deana, *Photochem. Photobiol.* **2012**, *88*, 1211.

[53] B. Alince, P. Lepoutre, *J. Colloid Interface Sci.* **1980**, *76*, 182.

[54] P. Naglič, M. Bürmen, B. Likar, Y. Zelinskyi, *Biomed. Opt. Express* **2020**, *11*, 1901.

[55] B. Christ, M. Marhic, in *Emerging Optical Materials*, SPIE, Bellingham, Washington, USA **1982**, pp. 169–172.

[56] T. T. A. Nguyen, H. N. D. Le, M. Vo, Z. Wang, L. Luu, J. C. Ramella-Roman, *Biomed. Opt. Express* **2012**, *3*, 1200.

[57] X. Zhang, J. Qiu, J. Qiu, J. Qiu, X. Li, X. Li, J. Zhao, J. Zhao, L. Liu, L. Liu, *Appl. Opt.* **2020**, *59*, 2337.

[58] S. N. Kasarova, N. G. Sultanova, C. D. Ivanov, I. D. Nikolov, *Opt Mater (Amst)* **2007**, *29*, 1481.

[59] C. D. Mobley, in *Handbook of Optics*, 2nd ed. (Ed: M. Bass), McGraw-Hill, New York, US **1994**.

[60] V. T. Hoang, G. Stępniewski, K. H. Czarnecka, R. Kasztelanic, V. C. Long, K. D. Xuan, L. Shao, M. Śmietana, R. Buczyński, *Appl. Sci.* **2019**, *9*, 1145.

[61] O. Miniver, P. Kalpana, S. Perez, N. Holtz, S. Udayashankar, T. Dale, *3D Tumor Spheroid Invasion Monitoring with Live-Cell Analysis*, **2020**, accessed on: May, 2024, https://www.news-medical.net/whitepaper/20200714/3D-Tumor-Spheroid-Invasion-Monitoring-with-Live-Cell-Analysis.aspx.

[62] M. Vinci, C. Box, M. Zimmermann, S. A. Eccles, *Methods Mol Biol* **2013**, *986*, 253.

[63] J. V. Cockle, S. Picton, J. Levesley, E. Ilett, A. M. Carcaboso, S. Short, L. P. Steel, A. Melcher, S. E. Lawler, A. Brüning-Richardson, *Br. J. Cancer* **2015**, *112*, 693.

[64] J. R. Wisñiewski, F. Z. Gaugaz, *Anal. Chem.* **2015**, *87*, 4110.

[65] D. B. Bekker-Jensen, A. Martínez-Val, S. Steigerwald, P. Rüther, K. L. Fort, T. N. Arrey, A. Harder, A. Makarov, J. V. Olsen, *Mol. Cell. Proteomics* **2020**, *19*, 716.

[66] R. Bruderer, O. M. Bernhardt, T. Gandhi, S. M. Miladinović, L. Y. Cheng, S. Messner, T. Ehrenberger, V. Zanotelli, Y. Butscheid, C. Escher, O. Vitek, O. Rinner, L. Reiter, *Mol. Cell. Proteomics* **2015**, *14*, 1400.

[67] S. Tyanova, T. Temu, P. Sinitcyn, A. Carlson, M. Y. Hein, T. Geiger, M. Mann, J. Cox, *Nat. Methods* **2016**, *13*, 731.

[68] E. Eden, R. Navon, I. Steinfeld, D. Lipson, Z. Yakhini, *BMC Bioinformatics* **2009**, *10*, 48.

[69] R. J. Kinsella, A. Kähäri, S. Haider, J. Zamora, G. Proctor, G. Spudich, J. Almeida-King, D. Staines, P. Derwent, A. Kerhornou, P. Kersey, P. Flicek, *Database* **2011**, *2011*, bar030.

[70] F. Cunningham, J. E. Allen, J. Allen, J. Alvarez-Jarreta, M. R. Amode, I. M. Armean, O. Austine-Orimoloye, A. G. Azov, I. Barnes, R. Bennett, A. Berry, J. Bhai, A. Bignell, K. Billis, S. Boddu, L. Brooks, M. Charkhchi, C. Cummins, L. Da Rin Fioretto, C. Davidson, K. Dodiya, S. Donaldson, B. El Houdaigui, T. El Naboulsi, R. Fatima, C. G. Giron, T. Genez, J. G. Martinez, C. Guijarro-Clarke, A. Gymer, et al., *Nucleic Acids Res.* **2022**, *50*, D988.

[71] M. Franz, C. T. Lopes, D. Fong, M. Kucera, M. Cheung, M. C. Siper, G. Huck, Y. Dong, O. Sumer, G. D. Bader, *Bioinformatics* **2023**, *39*, btad031.

[72] H. Schlichting, *Boundary-8393layer theory*, Vol. *121*, McGraw-Hill, New York, US **1961**.

[73] J. P. Holman, *Heat Transfer (Si Units)*, Tata McGraw Hill Education Private Limited, New York, US **2011**.

[74] D. Katritsis, L. Kaiktsis, A. Chaniotis, J. Pantos, E. P. Efstathopoulos, V. Marmarelis, *Prog Cardiovasc Dis* **2007**, *49*, 307.

[75] M. Montorsi, G. G. Genchi, D. De Pasquale, G. De Simoni, E. Sinibaldi, G. Ciofani, *Biotechnol. Bioeng.* **2022**, *119*, 1965.

[76] Y. Perez-Riverol, J. Bai, C. Bandla, D. García-Seisdedos, S. Hewapathirana, S. Kamatchinathan, D. J. Kundu, A. Prakash, A. Frericks-Zipper, M. Eisenacher, M. Walzer, S. Wang, A. Brazma, J. A. Vizcaíno, *Nucleic Acids Res.* **2022**, *50*, D543.